π–π interaction between metal–organic framework and reduced graphene oxide for visible-light photocatalytic H2 production.

KARTHIK, P., VINOTH, R., ZHANG, P., CHOI, W., BALARAMAN, E. and NEPPOLIAN, B.

2018

ACS APPLIED ENERGY MATERIALS
Cite This: ACS Appl. Energy Mater. XXXX, XXX, XXX−XXX
Article
www.acsaem.org

π−π Interaction Between Metal−Organic Framework and Reduced Graphene Oxide for Visible-Light Photocatalytic H_2 Production

Peramaiah Karthik,[†] Ramalingam Vinoth,[†] Peng Zhang,[§] Wonyong Choi,[§] Ekambaram Balaraman,*[,‡] and Bernaurdshaw Neppolian*[,†]

[†]SRM Research Institute, SRM University, Kattankulathur, Chennai 603203, Tamil Nadu, India
[‡]Catalysis Division, CSIR-National Chemical Laboratory (CSIR-NCL), Dr. Homi Bhabha Road, Pune 411008, India
[§]Division of Environmental Science and Engineering, Pohang University of Science and Technology (POSTECH), Pohang 37673, Korea

Supporting Information

ABSTRACT: Solar water splitting provides a promising path for sustainable hydrogen production and solar energy storage. In recent times, metal−organic frameworks (MOFs) have received considerable attention as promising materials for diverse solar energy conversion applications. However, their photocatalytic performance is poor and rarely explored due to rapid electron−hole recombination. Herein, we have developed a material MOF@rGO that exhibits highly enhanced visible-light photocatalytic activity. A real-time investigation reveals that a strong π−π interaction between MOF and rGO is responsible for efficient separation of electron−hole pairs, and thereby enhances the photocatalytic hydrogen production activity. Surprisingly, MOF@rGO showed ∼9.1-fold enhanced photocatalytic hydrogen production activity compared to that of pristine MOF. In addition, it is worth mentioning here that remarkable apparent quantum efficiency (0.66%) is achieved by π−π interaction mediated charge carrier separation.

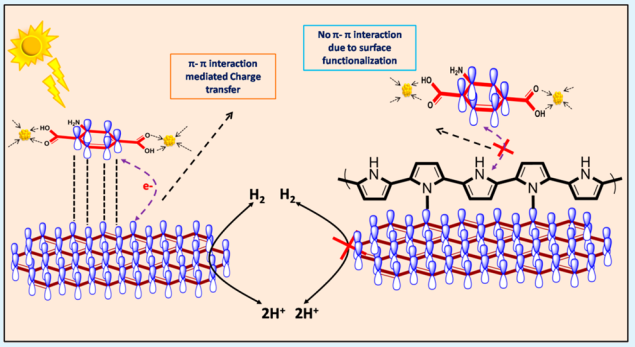

KEYWORDS: *metal−organic framework, π−π interaction, reduced graphene oxide, photocatalyst, hydrogen production*

INTRODUCTION

Increasing energy demand and undesirable environmental impacts created by fossil fuels have encouraged a search for abundant renewable energy resources. Hydrogen has been considered as a prime candidate as an alternative fuel due to zero emission and its high combustion energy. Hydrogen can be produced from renewable sources including water utilizing nuclear, wind, or solar energy. The conversion of solar energy into chemical energy through solar hydrogen production by artificial photosynthesis is a highly promising approach, but an equally complex problem. A facile and sustainable approach to producing hydrogen is that photocatalytic water splitting uses semiconductor metal oxides photocatalysts.[1−3] At the same time, an equal importance has been given to the metal−organic frameworks (MOFs) because of their unique properties and also because they are a new hybrid material for photocatalytic applications.[4−9] However, rational design and development of new materials for solar hydrogen production is extremely challenging and has recently gained great interest in contemporary science.

Metal−organic frameworks (MOFs) are a class of porous materials with attractive physiochemical properties such as high surface area, tunable architecture, and tunable pore structure. These properties endow MOFs with great potential applications in selective gas separation and adsorption, gas storage, optical materials, sensor applications, drug delivery, photovoltaic device, and photocatalysis.[10−14] However, due to poor light-harvesting ability, low charge carrier mobility, and reduced carrier separation, utilization of MOFs for photocatalytic applications is very limited.[15] In recent times, notable strategies have been developed for the improvement of the photocatalytic performance of MOFs.[16,17] Notably, limited examples are known for graphene supported MOFs composite materials as a photocatalyst[18−20] for solar light conversion to chemical energy.

Graphene is a two-dimensional single sheet made up of hexagonally packed carbon atoms with interesting optoelectronic properties. There are different approaches to synthesizing graphene-based MOFs[21−23] (Figure 1 a). The decoration of a graphene sheet with MOF assemblies indeed minimizes the charge recombination and also facilitates the charge carrier separation and transportation.[23,24] Of late, Ti-based MOFs have attracted much attention owing to its simple synthetic protocol, high chemical stability, and good light-harvesting ability. Thus,

Received: December 8, 2017
Accepted: April 19, 2018
Published: April 19, 2018

DOI: 10.1021/acsaem.7b00245
ACS Appl. Energy Mater. XXXX, XXX, XXX−XXX

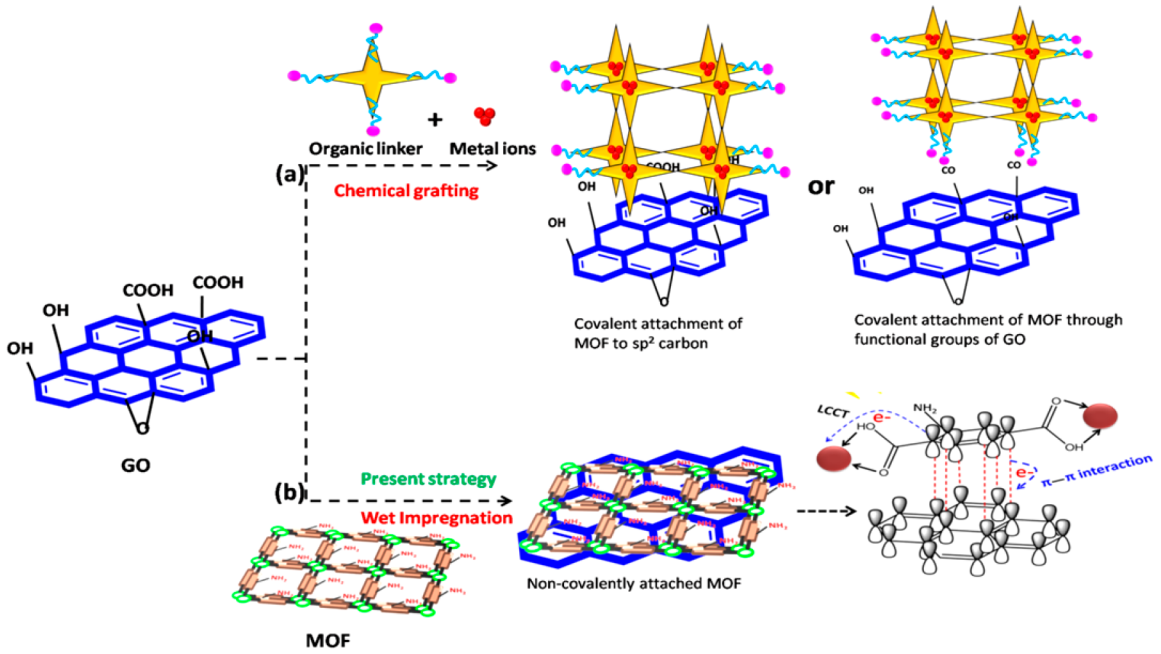

Figure 1. (a) Synthesis of graphene-based MOF hybrid materials by chemical grafting strategy. (b) Wet impregnation method to synthesize graphene-based MOF with strong $\pi-\pi$ interaction (our approach).

Ti-based MOF along with cocatalysts such as Pt and Au has been utilized as a photocatalyst for application such as H_2 production, Cr(VI) reduction, and CO_2 hydrogenation.[25,26] In contrast, the NH_2-MIL-125(Ti) MOF without cocatalyst shows a lower photocatalytic activity due to rapid electron−hole pair recombination. To overcome this issue, we have introduced graphene oxide as a solid support to enhance the photocatalytic activity without using any noble metals and cocatalyst. On the other hand, it is known that the functionalization of the organic molecule on graphene oxide may lead to either a covalent or noncovalent interaction.[27−29] In the covalent interaction, due to the covalent bond formation between organic molecules with sp^2 carbon, (—C═C—)/oxygen functional groups of graphene strongly disturb the extended π-conjunction and alter its electronic properties. Also, the covalent interaction of graphene changes their hybridization state from sp^2 to sp^3 and induces the insulating behavior.[30,31] As a consequence of change in the hybridization, the charge carrier mobility of graphene decreased. In contrast to covalent functionalization, noncovalent functionalization offers a strong interaction with organic molecule without affecting the extended π-conjunction of graphene.[32,33]

In this present study, we have successfully fabricated a noncovalently anchored photoactive NH_2-MIL-125(Ti)/rGO MOF by a simple wet impregnation method (Figure 1b). Prominently, noncovalently attached NH_2-MIL-125(Ti)/rGO MOF showed strong $\pi-\pi$ interactions. To the best of our knowledge, the $\pi-\pi$ interactions and their role in the charge transfer process have not been studied in rGO/metal−organic framework composite materials. Interestingly, the $\pi-\pi$ interactions facilitate the interfacial charge transfer process and thereby enhance the visible-light photocatalytic hydrogen production activity. Moreover, the $\pi-\pi$ interaction between NH_2-MIL-125(Ti) and rGO was extensively studied using various spectroscopic techniques.

EXPERIMENTAL SECTION

Methods. The synthesized MOF photocatalyst was characterized using the following spectroscopic techniques. The crystallinity was confirmed via X-ray diffraction (XRD) patterns using Cu Kα radiation (PANalyticalX'pert powder diffractometer) (λ = 1.5418 Å). The morphological studies were carried out by using field emission-scanning electron microscopy (FEI Quanta FEG 200 HR-SEM). The optical absorption properties were assessed with UV−vis spectrophotometer. The X-ray photoelectron spectrum (XPS) analysis was performed using a Shimadzu ESCA 3100. The surface area, pore size, and pore volume were determined using a Quanta chrome Nova-1000 surface analyzer via a nitrogen (N_2) adsorption−desorption process.

Synthesis of NH_2-MIL-125(Ti) MOF. The NH_2-MIL-125(Ti) MOF was synthesized by a solvothermal method. In brief, 2.4 mL of titanium tetra-isopropoxide (TTIP) and 2.2 g of 2-aminoterephthalic acid were added into the DMF−methanol mixture (36 and 4 mL). The resulting solution was transferred into a 100 mL Teflon-lined stainless-steel autoclave and heated at 150 °C for 48 h. After that, the resultant precipitate was collected by centrifugation and repeatedly washed with methanol to remove the unreacted DMF. Finally, the obtained powder was dried at 150 °C for 12 h to remove the residual 2-aminoterephthalic acid.

Synthesis of NH_2-MIL-125(Ti)/Reduced Graphene Oxide (rGO) MOF Hybrid. The reduced graphene oxide supported NH_2-MIL-125(Ti) MOF was synthesized using a simple wet impregnation method. Initially, the GO solution and NH_2-MIL-125(Ti) were prepared separately by following the reported procedure.[25] In a typical synthesis, an appropriate amount of GO (2, 4, 6, 8, and 10 wt %) was added to 40 mL of ethanol and ultrasonicated for 2 h in a low frequency ultrasonicator (20 kHz, continuous mode, amplitude 30%). Subsequently, 300 mg of NH_2-MIL-125(Ti) was homogeneously dispersed in water, and then, GO solution was added to the MOF solution. Then, the resultant yellow colloidal suspension was sonicated for 15 min (20 kHz, low frequency ultrasonicator, continuous mode, amplitude 30%). The resulting mixture was predried in a hot plate, and the resultant impregnated powder was dried in an oven at 180 °C for 24 h.

Photocatalytic Hydrogen Production. The photocatalytic H_2 production experiments were performed using a 100 mL Pyrex glass cylinder reactor and a 300 W Xe-lamp (Oriel Instruments-Newport) used as a light source. In a typical procedure, a 30 mg portion of

DOI: 10.1021/acsaem.7b00245
ACS Appl. Energy Mater. XXXX, XXX, XXX−XXX

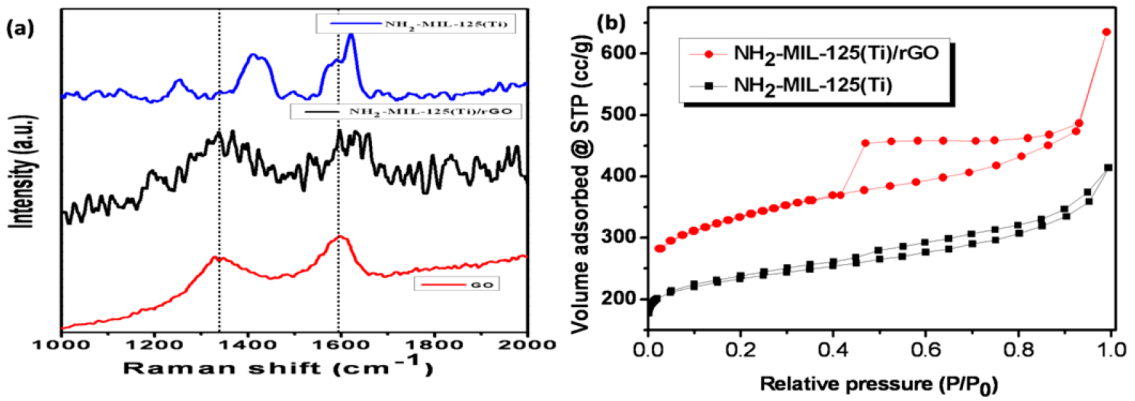

Figure 2. (a) Raman spectra of rGO, NH_2-MIL-125(Ti), and NH_2-MIL-125(Ti)/rGO MOFs. (b) Nitrogen adsorption−desorption isotherms of NH_2-MIL-125(Ti) and NH_2-MIL-125(Ti)/rGO MOFs.

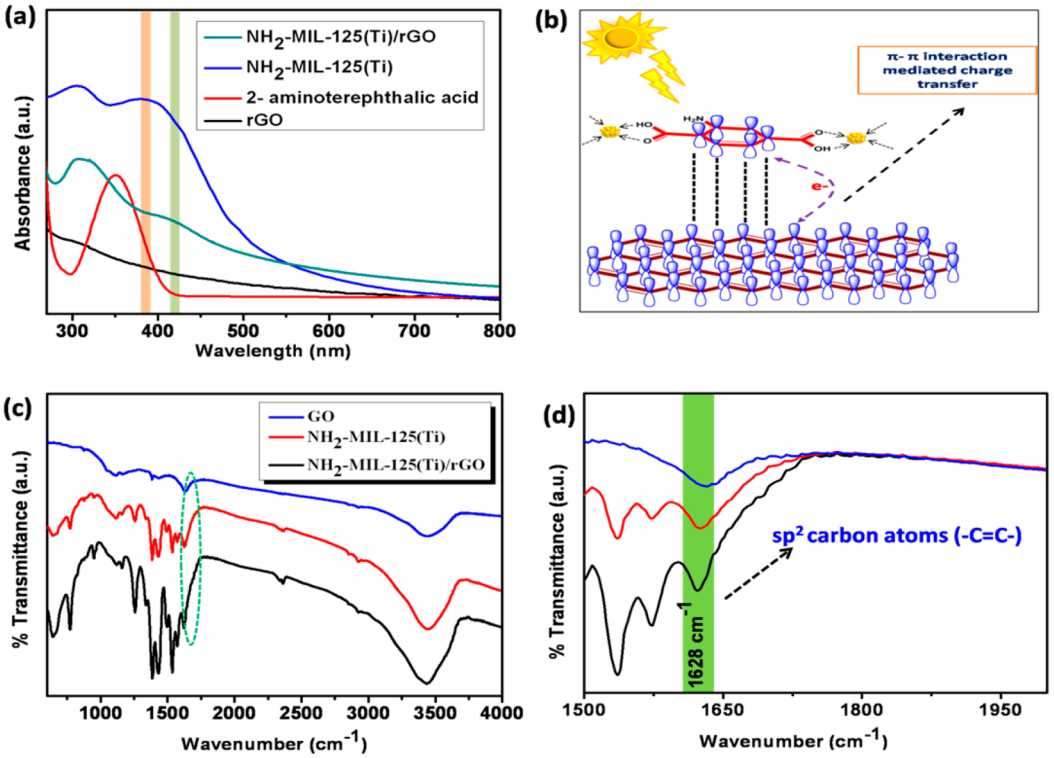

Figure 3. (a) UV−vis absorbance spectra of rGO, 2-aminoterephthalic acid, NH_2-MIL-125(Ti), and NH_2-MIL-125(Ti)/rGO. (b) Mechanism for $\pi-\pi$ interaction between rGO and NH_2-MIL-125(Ti) MOF. (c) FTIR spectra of GO and NH_2-MIL-125(Ti) and (d) NH_2-MIL-125(Ti)/rGO (enlarged spectrum).

photocatalyst and 30 mL of 5% aqueous TEOA solutions were taken in a reactor. The resulting solution was evacuated at room temperature to remove the oxygen content. Subsequently, high purity N_2 gas was purged for 30 min to remove the dissolved oxygen present in the reaction mixture. After that, the whole mixture was irradiated with a 300 W Xe-lamp using a UV filter. For the quantification of the liberated H_2 gas, the H_2 gas was collected from the reactor using a GC syringe and analyzed by off-line gas chromatograph with a TCD detector (Shimadzu GC-2014 with molecular sieve/5 Å column) using N_2 as a carrier gas at a regular time interval.

RESULTS AND DISCUSSION

Structural Studies. The XRD patterns of NH_2-MIL-125(Ti) and NH_2-MIL-125(Ti)/rGO MOFs are displayed in Figure S1. These clearly show that NH_2-MIL-125(Ti) and NH_2-MIL-125(Ti)/rGO MOFs exhibited identical XRD patterns which matched with literature reports, which indicated the formation of NH_2-MIL-125(Ti) MOF when 2-amino-terephthalic acid was utilized as an organic linker.[34,35] The incorporation of the NH_2-MIL-125(Ti) MOF into the rGO does not influence the crystal lattice of the existing structure. Moreover, no characteristic diffraction peaks related to TiO_2 phases such as anatase and rutile were observed, and this clearly emphasized that the framework is constructed by a small titanium−oxo cluster and not by bulk TiO_2. The diffraction peak that corresponds to rGO was also absent due to the low wt % of rGO loading, and the trace peak was masked by the high intensity peak of MOF.[36,37]

The Raman spectra of NH_2-MIL-125(Ti), NH_2-MIL-125(Ti)/rGO, and GO are shown in Figure 2a. The characteristic peak of rGO was observed at 1348 and 1600 cm^{-1}, mainly attributed to D and G bands, respectively.[38,39]

DOI: 10.1021/acsaem.7b00245
ACS Appl. Energy Mater. XXXX, XXX, XXX−XXX

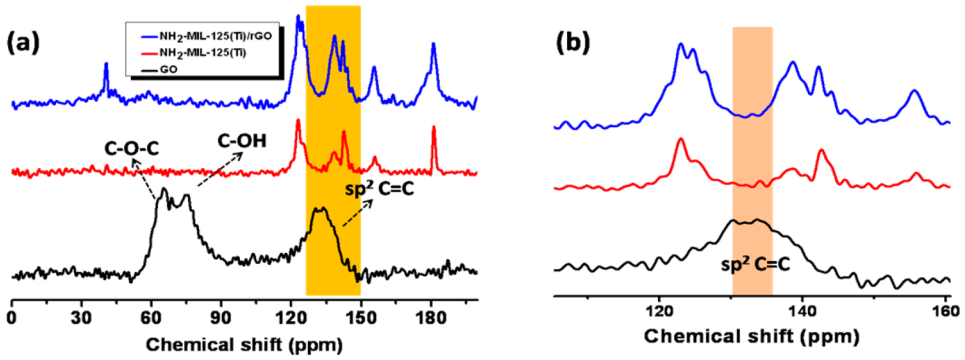

Figure 4. (a) Solid-state ^{13}C NMR spectra of rGO, NH_2-MIL-125(Ti), and NH_2-MIL-125(Ti)/rGO. (b) Enlarged spectra of rGO, NH_2-MIL-125(Ti), and NH_2-MIL-125(Ti)/rGO (100−160 ppm).

The NH_2-MIL-125(Ti) MOF exhibits peaks at 1500 and 1620 cm^{-1} corresponding to the C−C and N−H bond bending vibrations of the organic linker.[40] In addition, the peaks located at 1245 and 1414 cm^{-1} are related to the bending and symmetric stretching of a Ti−O framework. This result supports the −COOH group of the organic linker being directly connected to the Ti−oxo cluster.[41] However, the increase in D band intensity and a shift in the G band of NH_2-MIL-125(Ti)/rGO are not only due to the reduction of GO but also due to the successful incorporation of NH_2-MIL-125(Ti) on an rGO sheet.

Figure 2b illustrates the N_2 adsorption−desorption isotherms of NH_2-MIL-125(Ti) and optimized NH_2-MIL-125(Ti)/rGO MOFs. The surface area, pore volume, and pore size of NH_2-MIL-125(Ti) and NH_2-MIL-125(Ti)/rGO MOFs are summarized in Table S1. As depicted in Figure 2b, the pure NH_2-MIL-125(Ti) MOF follows the typical type I isotherm pattern similar to that of zeolites and zeolite-like crystalline materials according to the IUPAC taxonomy.[42] The measured surface area and pore volume of NH_2-MIL-125(Ti) are 710 $m^2\ g^{-1}$ and 0.649 cc/g, whereas rGO (6 wt %) loaded NH_2-MIL-125(Ti) MOF exhibits a type IV isotherm pattern with 962 $m^2\ g^{-1}$ surface area and 0.266 cc/g pore volume. This clearly demonstrates that the introduction of rGO has significantly enhanced the surface area of a NH_2-MIL-125(Ti) MOF. Nonetheless, the pore volume of NH_2-MIL-125(Ti)/rGO (6 wt %) decreased from 0.649 to 0.266 cc/g nm, and it might due to pores blocked by rGO during the effective wet impregnation.

Elaboration of Strong $\pi-\pi$ Interaction between NH_2-MIL-125(Ti) MOF and rGO. To study the electronic interactions between NH_2-MIL-125(Ti) MOF and rGO, a UV−vis absorbance analysis was performed, and the results are shown in Figure 3a. It is evident from Figure 3a that the peak appeared for the free organic linker at 352 nm is mainly due to the $\pi-\pi^*$ transition. After the MOF formation with an organic linker, the peak at 352 nm was shifted to 329 nm and revealed the coordination between the linker and Ti−oxo cluster.[43] Very importantly, after incorporation of the NH_2-MIL-125(Ti) MOF with rGO, the characteristic peak of NH_2-MIL-125(Ti) MOF at 380 nm[44] shifted to 415 nm. It shows the existence of electronic transition between NH_2-MIL-125(Ti) MOF and rGO. However, we sought to know how the electronic transition occurred between rGO and MOF. With this, in order to study whether the electronic transition occurred through any covalent interaction or not, the FTIR analysis was carried out. As shown in Figure 3c, d, the FTIR spectra of rGO, NH_2-MIL-125(Ti), and NH_2-MIL-125(Ti)/rGO exhibit the characteristic peak of C═C bonds at 1628 cm^{-1}.[45,46] The peak intensity of sp^2 carbon atoms is increased in the order NH_2-MIL-125(Ti)/rGO > NH_2-MIL-125(Ti) > rGO. It is interesting to note that, compared to rGO and NH_2-MIL-125(Ti) MOF, rGO supported NH_2-MIL-125(Ti) shows a higher sp^2 carbon atom intensity due to the coexistence of sp^2 carbons (from the aromatic ring of 2-aminoterephthalic acid). In general, incorporation of organic molecules on rGO can occur either covalently or noncovalently ($\pi-\pi$). The covalent attachment of an organic linker strongly perturbs the extended aromatic character of rGO by transformation of carbon atoms from sp^2 to sp^3 hybridization, which results in a decrease in the sp^2 —C═C— stretching frequency.[47,48] However, in this case, the peak intensity of sp^2 carbon atoms is increased. These results clearly reveal the lack of covalent interaction between rGO and NH_2-MIL-125(Ti) MOF. In addition, the peaks located at 1386, 1170, and 1049 cm^{-1} are mainly attributed to stretching and bending vibrations of —OH, —COOH, and C—OH, respectively.[49] Furthermore, NH_2-MIL-125(Ti) and NH_2-MIL-125(Ti)/rGO show the absorption band at 3438 cm^{-1}, which is assigned to the asymmetry stretching vibration of a primary amine group. The peak centered at 1261 cm^{-1} is ascribed to the N—C stretching vibration. It is revealed that rGO did not influence the amine group of the organic linker and the nature of the amine group is unchanged after successful incorporation into the rGO matrix which further supports the lack of covalent interaction. Therefore, above all, the results undoubtedly demonstrate that existence of strong nonconvent interactions between rGO and NH_2-MIL-125(Ti) MOF and this facilitates the electronic transition between rGO and NH_2-MIL-125(Ti) MOF. However, the only possibility of electronic transition between rGO and NH_2-MIL-125(Ti) MOF is the direct excitation of π-electrons from the π-orbital of the NH_2-MIL-125(Ti) MOF to rGO. Hence, the shift in absorbance peak is due to strong $\pi-\pi$ interaction mediated electronic transitions, and the possible orientation of the π-orbital is given in Figure 3b. Similarly, there are a few literature precedents also known for the shift in the UV−vis absorbance spectra for $\pi-\pi$ interactions.[50,51] In addition, the strong $\pi-\pi$ interactions facilitate fast electron transport and reduce the electron−hole pair recombination as identified from PL and lifetime decay studies, thereby enhancing the photocatalytic H_2 production activity.

Moreover, in order to further confirm the $\pi-\pi$ interactions, we have performed the solid-state ^{13}C NMR study. As depicted in Figure 4, the chemical shift values of both NH_2-MIL-125(Ti) MOF and rGO are well-matched with the previously reported

DOI: 10.1021/acsaem.7b00245
ACS Appl. Energy Mater. XXXX, XXX, XXX−XXX

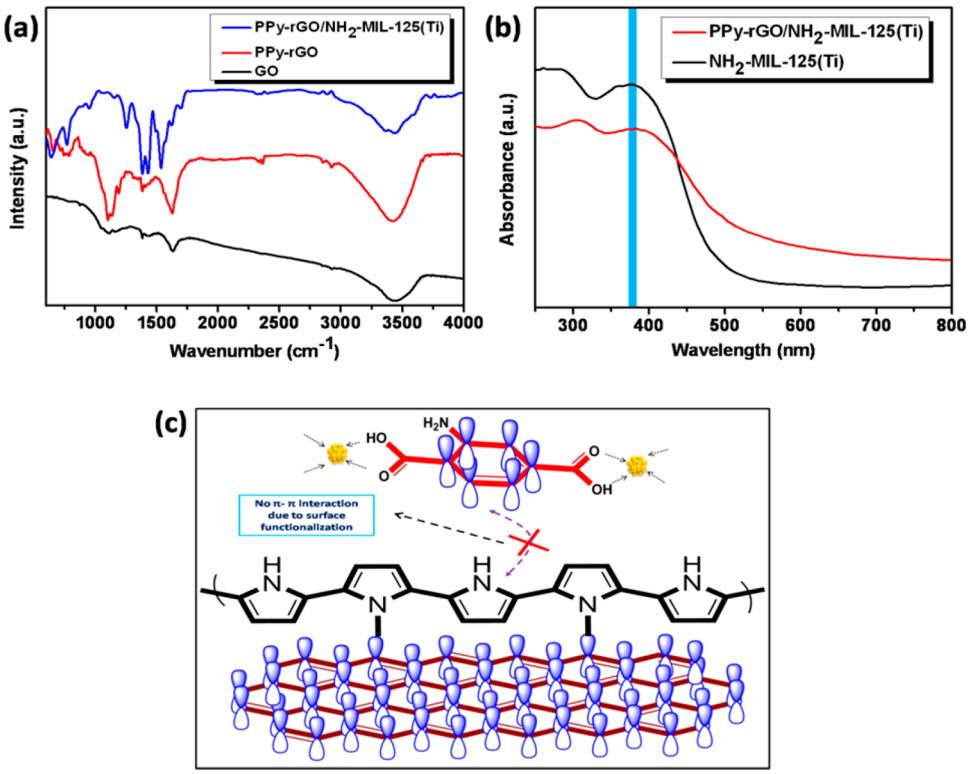

Figure 5. (a, b) FTIR and UV−vis absorbance spectra of GO, APTES-rGO, and NH_2-MIL-125(Ti)/APTES-rGO. (c) Schematic diagram of prevention of direct $\pi-\pi$ interaction between rGO and NH_2-MIL-125(Ti) MOF by APTES functionalization.

literature.[52,53] After incorporation of rGO with NH_2-MIL-125(Ti) MOF, the characteristic chemical shift of sp^2 carbons for rGO at ∼132 ppm shifted to ∼138 ppm. The upfield shift is due to decreasing electron density of sp^2 carbons by migration of charge through the $\pi-\pi$ stacking interactions and makes sp^2 carbons relatively deshielded. This result confirmed the existence of a $\pi-\pi$ interaction between rGO and NH_2-MIL-125(Ti) MOF. Similarly, Han et al. also proved the $\pi-\pi$ interactions by ^1H NMR shift.[54]

Subsequently, to authenticate the strong $\pi-\pi$ interaction and charge transfer process between rGO and NH_2-MIL-125(Ti) MOF, we have designed a simple architecture using polypyrrole. In this, to protect the direct contact between rGO and NH_2-MIL-125(Ti) MOF, GO was functionalized with polypyrrole. By using polypyrrole modified rGO as a platform, NH_2-MIL-125(Ti)/PPy-rGO MOFs were synthesized by a wet impregnation method. The effective surface functionalization of PPY on rGO was studied by FTIR spectra. As shown in Figure 5a, along with the characteristic vibrations of GO, PPy-rGO has new vibrations at 1556 and 1466 cm^{-1} related to the pyrrole ring,[55] which reveal the effective functionalization of PPy on rGO. It is important to note that no significant shift was observed in the main absorbance peak of the NH_2-MIL-125(Ti) MOF at 380 nm in contrast with that of the NH_2-MIL-125(Ti) MOF/rGO MOF as depicted in Figure 5b. It can be inferred that the functionalization of PPy screened the direct contact of the π-orbital of both rGO and NH_2-MIL-125(Ti) MOF and shielded the $\pi-\pi$ interactions. On the other hand, a nominal (5 nm) red shift was observed for NH_2-MIL-125(Ti)/PPy-rGO MOF; this might be due to interaction between PPy and rGO. The probable scheme for noncontact between rGO and NH_2-MIL-125(Ti) MOF is illustrated in Figure 5c. In addition, the photocatalytic H_2 production reaction was also performed with the NH_2-MIL-125(Ti)/PPY-rGO MOF under identical conditions. As we expected, no H_2 was evolved (Figure S2). This is mainly due to the lack of $\pi-\pi$ interaction and the screening of the photogenerated electron transfer process between rGO and NH_2-MIL-125(Ti) MOF by PPy. Thus, all of the above results indisputably proved the strong $\pi-\pi$ interaction between rGO and NH_2-MIL-125(Ti) MOF.

In addition, we synthesized the same rGO supported NH_2-MIL-125(Ti) MOF by the hydrothermal method to compare the $\pi-\pi$ interaction with MOF synthesized by the wet impregnation method. It was noted that the hydrothermally synthesized NH_2-MIL-125(Ti)/rGO MOF did not show an absorption peak at 415 nm corresponding to the $\pi-\pi$ interaction (Figure S3a). In the FTIR spectra (Figure S3b), the intensity of characteristic vibration of aromatic C═C is extremely diminished compared to that of GO and NH_2-MIL-125(Ti)/rGO MOF synthesized from the wet impregnation method. One can infer that, during hydrothermal synthesis of NH_2-MIL-125(Ti) MOF, GO might be converted into rGO and thereby decrease the sp^2 hybridized carbon atom (C═C) intensity. In addition, this also affects the NH_2-MIL-125(Ti) MOF formation and decreases the sp^2 hybridized carbon atom (C═C) intensity. This indicates that the wet impregnation synthesis of NH_2-MIL-125(Ti)/rGO MOF could not affect the 2-amino terephthalic acid and facilitates the strong $\pi-\pi$ interaction. Furthermore, the photocatalytic H_2 production reaction was also performed with hydrothermally synthesized NH_2-MIL-125(Ti)/rGO MOF. Notably, no H_2 gas was produced under identical conditions (Figure S4).

EPR analysis was also performed to further demonstrate the $\pi-\pi$ interaction phenomena. The EPR spectra of NH_2-MIL-125(Ti)/rGO, NH_2-MIL-125(Ti), and rGO are shown in Figure 6. The sharp and narrow EPR peak was observed for GO

DOI: 10.1021/acsaem.7b00245
ACS Appl. Energy Mater. XXXX, XXX, XXX−XXX

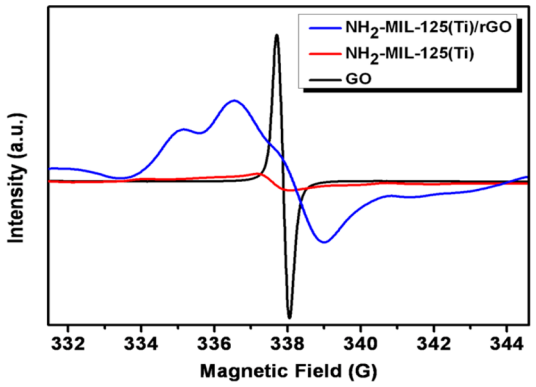

Figure 6. Room temperature EPR analysis of GO, NH_2-MIL-125(Ti), and NH_2-MIL-125(Ti)/rGO.

due to the localized spins caused by the nonbonding π-electrons which can be created at the edges of the graphene sheet.[56,57] However, after the incorporation of NH_2-MIL-125(Ti) with rGO, a broad peak appeared. This can be explained as the π-electrons at the edges of rGO extend their delocalization and exhibit rapid spin−lattice relaxation through $\pi-\pi$ interactions.[58] In addition, the EPR peak shift and splitting also supported the $\pi-\pi$ interaction. It might be due to the inclusion of rGO with NH_2-MIL-125(Ti) MOF which enhanced the spin−orbital coupling between rGO and NH_2-MIL-125(Ti) through noncovalent interactions.[59,60]

The chemical oxidation state and electronic structure of prepared NH_2-MIL-125(Ti) MOF and NH_2-MIL-125(Ti)/rGO MOF were studied through XPS analysis. As shown in Figure 7, the NH_2-MIL-125(Ti) MOF exhibits binding energy peaks such as 282.5, 284.5, 286.1, and 288.2 eV which correspond to Ti—C, sp^2 carbon (C═C), C—N, and C═O bonds, respectively. Similarly, the NH_2-MIL-125(Ti)/rGO MOF also showed the same C 1s peaks. However, the sp^2 carbon binding energy of the NH_2-MIL-125(Ti)/rGO MOF shifted by 0.3 eV toward low binding energy compared to NH_2-MIL-125(Ti) MOF due to the high electron density around the organic linker.[61] This revealed that the insertions of rGO extend the π-conjugation to MOF through the $\pi-\pi$ interaction and significantly increase the electron density around the organic linker as reliably seen with EPR spectra which further support the $\pi-\pi$ interaction. Moreover, as was seen from Table S2, the pristine MOF showed ~30.66% C═C bonds, whereas ~40.78% C═C was observed in the case of rGO/NH_2-MIL-125(Ti). This result clearly indicates that inclusion of graphene oxide increased the C═C bond intensity as is consistent with FTIR spectra. In addition, the N 1s spectra of NH_2-MIL-125(Ti) and NH_2-MIL-125(Ti)/rGO MOFs showed the binding energy of the —NH_2 group at 399.8 and 399.4 eV, respectively.[56] Notably, similar to the C 1s spectra, the binding energy of —NH_2 is also shifted by 0.4 eV toward low binding energy and supplements the strong $\pi-\pi$ interaction between rGO and the NH_2-MIL-125(Ti) MOF.

The morphology of synthesized MOFs was characterized by using TEM analysis. As shown in Figure 8, the pristine NH_2-MIL-125(Ti) exhibits a well-defined cubic nanostructure with homogeneous distribution, whereas NH_2-MIL-125(Ti)/rGO showed a layered nanostructure due to the presence of the rGO matrix. It can be seen that rGO has been utilized as a 2D platform for the formation of the layered structure. In addition, the successful embedding of MOF on the rGO sheet was confirmed by using STEM and EDX mapping (Figure 9). This also provides clear evidence for the uniform distribution of MOF on the rGO sheet. Moreover, embedding of MOF on the rGO sheet does not change the morphology of MOF, which

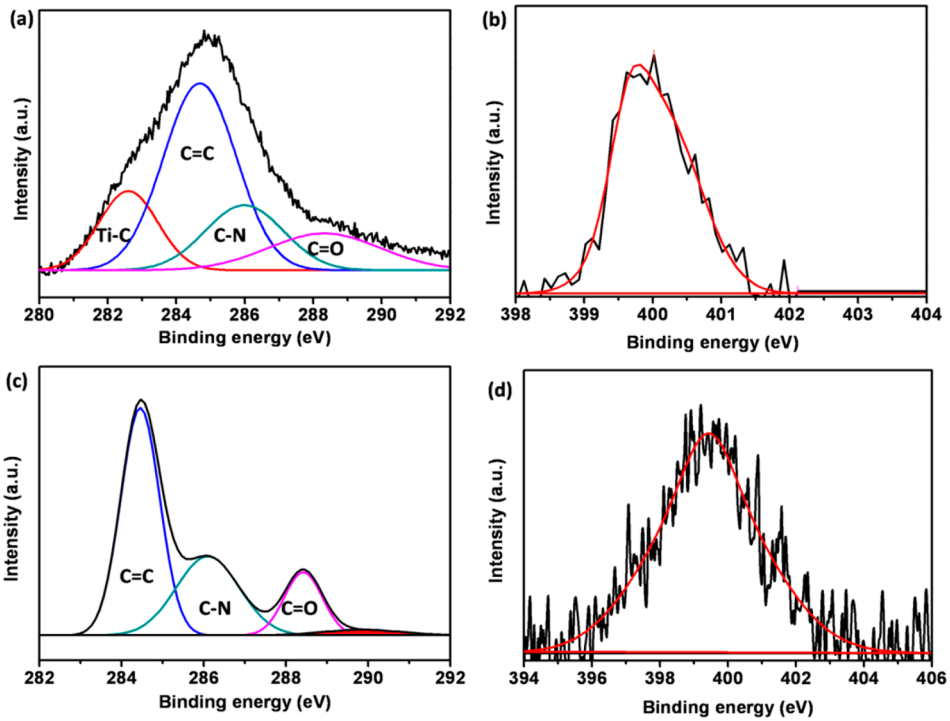

Figure 7. (a, c) High resolution C 1s spectra of NH_2-MIL-125(Ti) and NH_2-MIL-125(Ti)/rGO MOF. (b, d) N 1s spectra of NH_2-MIL-125(Ti) and NH_2-MIL-125(Ti)/rGO.

DOI: 10.1021/acsaem.7b00245
ACS Appl. Energy Mater. XXXX, XXX, XXX−XXX

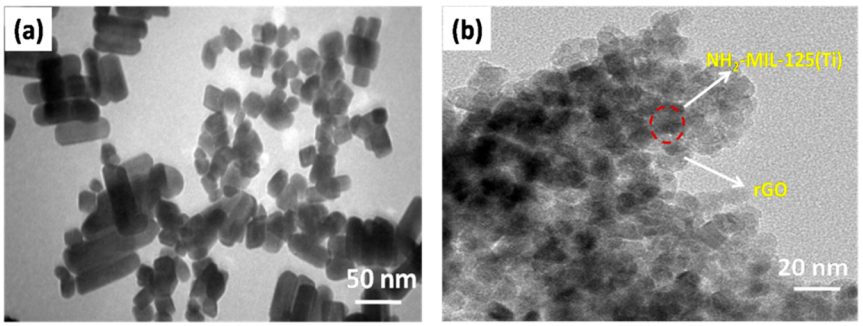

Figure 8. TEM images of (a) NH_2-MIL-125(Ti) and (b) NH_2-MIL-125(Ti)/rGO MOFs.

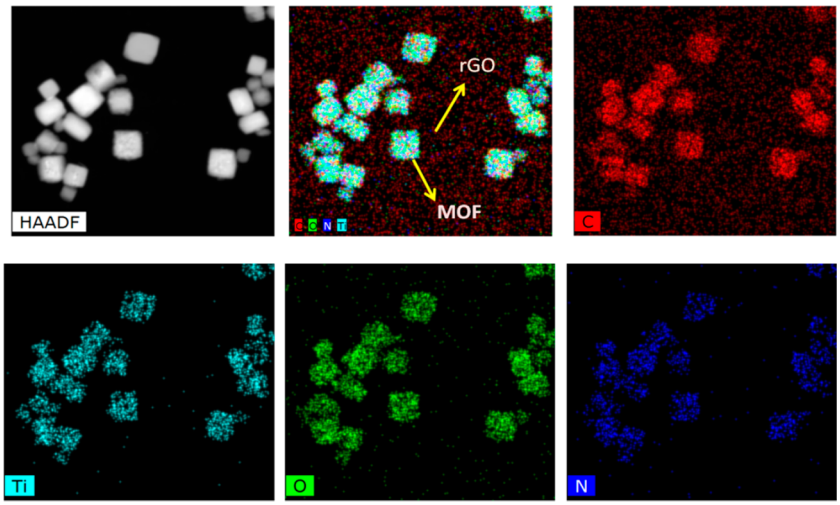

Figure 9. HAADF-STEM and C, Ti, O, and N elemental mappings of NH_2-MIL-125(Ti)/rGO.

confirms the noncovalent attachment of MOF on the rGO sheet, consistent with TEM and FTIR.

Photocatalytic Hydrogen Production. The above observations clearly reveal the existence of a strong $\pi-\pi$ interaction between rGO and NH_2-MIL-125(Ti) MOF. Inspired by the strong $\pi-\pi$ interactions, we studied the role of the $\pi-\pi$ interaction in photocatalytic H_2 production. Photocatalytic activities of all synthesized metal−organic framework photocatalysts were evaluated under visible-light irradiation. The controlled experiment (in the absence of light) showed no production of H_2 under dark conditions, which suggested that the water splitting reaction occurred only by the photocatalytic process. Figure 10a illustrates the amount of H_2 produced for the time using various photocatalysts. The relative order of photocatalytic water splitting by different rGO loaded NH_2-MIL-125(Ti) MOFs is as follows: 6 wt % > 8 wt % > 10 wt % > 4 wt % > 2 wt %. The corresponding amounts of H_2 produced are 91, 67, 66, 50, and 35 μmol h^{-1} g cat^{-1}, respectively. The pristine NH_2-MIL-125(Ti) MOF showed deficient H_2 production (7 μmol h^{-1} g cat^{-1}) due to high charge recombination and a reduced interfacial charge transfer process. The enhancement in the photocatalytic activity of the rGO loaded NH_2-MIL-125(Ti) MOF is due to $\pi-\pi$ interaction mediated superior charge carrier separation capability of rGO as revealed from PL spectra. However, the maximum H_2 production was achieved with 6 wt % rGO loaded NH_2-MIL-125(Ti) MOF. Further loading of rGO decreased the photocatalytic H_2 production. This can be explained as the higher amount of rGO increases the rate of recombination instead of charge carrier separation and thereby reduces the photocatalytic activity.[14] In addition, the excessive rGO loading (10 and 8 wt %) shields the incident light absorption ability of NH_2-MIL-125(Ti) MOF and thereby significantly reduces the photocatalytic activity.[62] Moreover, the rate constants of photocatalytic H_2 production for all the prepared photocatalysts were calculated, and the corresponding rate constant values are summarized in Table S3. The rate constant values revealed that the photocatalytic H_2 evaluation reaction follows typical Langmuir−Hinshelwood first order kinetics. Among all MOF photocatalysts, 6 wt % rGO loaded NH_2-MIL-125(Ti) MOF shows the highest rate constant value (k = 0.74 min^{-1}), and it was found to be the optimized catalyst. The obtained results, compared with results from some previously reported MOF-based photocatalysts, are summarized in Table S4. It is noted from Table S4 that the RhB/Pt@UiO-66 (Zr)-100 catalyst showed higher H_2 production. However, they have used high cost Pt metal nanoparticles in the composite; nevertheless, indeed the present catalyst avoids the use of noble metals and also showed comparable H_2 production performance (91 μmol h^{-1} g cat^{-1}). In addition, the apparent quantum efficiency (AQE) of 6 wt % rGO loaded photocatalyst was found to be 0.66%. This is the highest AQE compared with noble metal free MOF-based photocatalysts (Table S4). The recyclability experiments were carried out under similar conditions by evacuating generated gas at a fixed time interval for the next cycle, and the results are given in Figure 10b. It can be seen that consistent H_2 production was observed for 3 cycles without a significant decrease in the photocatalytic activity, and

DOI: 10.1021/acsaem.7b00245
ACS Appl. Energy Mater. XXXX, XXX, XXX−XXX

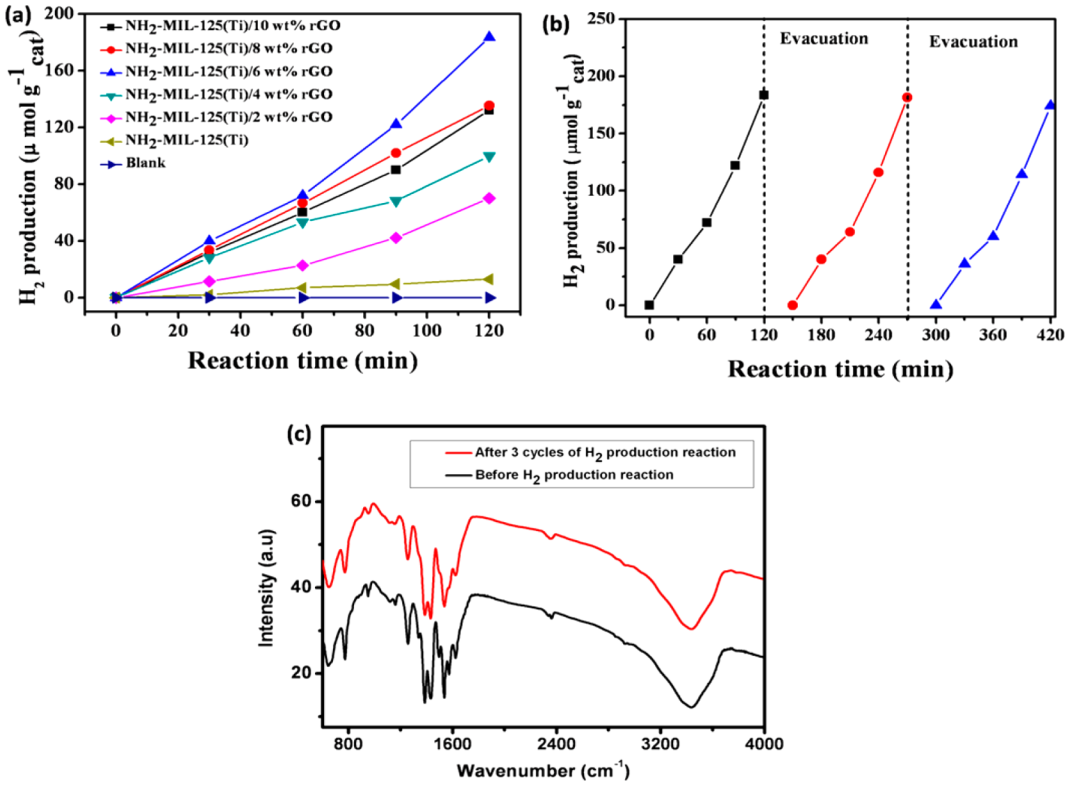

Figure 10. (a) Photocatalytic production of H_2 using different NH_2-MIL-125(Ti)/rGO-based MOFs under visible-light illumination. (b) Recycling test of photocatalytic production of H_2 using NH_2-MIL-125(Ti)/6.0 wt % rGO MOF. (c) FTIR spectra of NH_2-MIL-125(Ti)/rGO MOF (after and before photocatalytic H_2 production reactions).

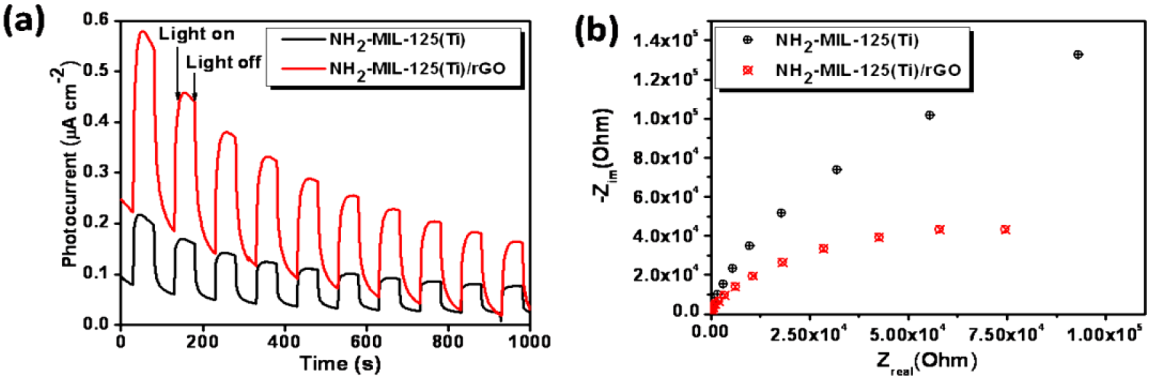

Figure 11. (a) Photocurrent responses with light on and off. (b) EIS Nyquist plots of NH_2-MIL-125(Ti) and NH_2-MIL-125(Ti)/rGO MOFs.

this indicates the high stability of NH_2-MIL-125(Ti)/rGO MOF photocatalyst. Furthermore, the stability of the metal–organic framework was confirmed by FTIR analysis (Figure 10c). There is no significant or drastic change observed in the existing stretching and bending frequencies of the metal–organic framework.

Charge-Separation and Photoelectrochemical Studies. The charge recombination processes of NH_2-MIL-125(Ti) and NH_2-MIL-125(Ti)/rGO MOFs were understood from the photoluminescence (PL) spectra and are shown in Figure S5a. The PL intensity of the rGO loaded NH_2-MIL-125(Ti) MOF is much lower than the pristine NH_2-MIL-125(Ti), which confirms the occurrence of effective charge separation and minimization in the charge recombination in the layered NH_2-MIL-125(Ti) via rGO support. We have also measured the lifetime of excited state charge carriers by using time-resolved transient fluorescence spectroscopy (Figure S5b). The fitted lifetimes of NH_2-MIL-125(Ti) and NH_2-MIL-125(Ti)/rGO are given in Table S5. The PL lifetime of NH_2-MIL-125(Ti) MOF is η^1 0.96 (A1 13.8%) and η^2 3.5 (A2 51.2%). On the other hand, the NH_2-MIL-125(Ti)/rGO MOF showed comparatively smaller lifetimes for excited state carriers, η^1 0.88 (A1 12.9%) and η^2 1.5 (A2 14.7%). The average lifetime in excited NH_2-MIL-125(Ti) and NH_2-MIL-125(Ti)/rGO samples is 2.2 and 0.97 ns, respectively. The shorter lifetime of excited state carriers in NH_2-MIL-125(Ti)/rGO MOF confirms the rapid photogenerated electron transfer through $\pi-\pi$ interaction, which thereby suppresses the electron–hole pair recombination and improves the rate of photocatalytic H_2 production activity.

To further demonstrate the role of rGO in the enhanced electron transport process through $\pi-\pi$ interactions, the

DOI: 10.1021/acsaem.7b00245
ACS Appl. Energy Mater. XXXX, XXX, XXX–XXX

photoelectrochemical analysis was studied by various electrochemical measurements. Figure 11a displays the transient photocurrent responses of pristine and optimized MOFs (6 wt % rGO/NH_2-MIL-125(Ti) MOF). It can be seen that the rGO loaded MOF showed ~2.8-fold enhancement in the photocurrent response than pristine MOF. This result clearly emphasized that the generation of light-induced charge carriers and the role of rGO in the rapid electron−hole pair's separation are consistent with the photoluminescence and time-resolved study. In order to get deeper insights on charge transfer resistance and the interfacial charge transport process through $\pi-\pi$ interactions, ESI analysis was performed, and results are depicted in Figure 11b. A well-defined semicircle was obtained for both pristine and rGO loaded MOFs. However, a smaller arc radius was observed for rGO loaded MOF compared with pristine MOF, and this suggests the smaller charge transfer resistance and rapid charge carrier separation of the rGO loaded MOF. Moreover, all the results undoubtedly confirmed the effective charge carrier separation through the $\pi-\pi$ interaction of rGO and facilitation of the enhanced photocatalytic H_2 production activity.

Photocatalytic H_2 Production Mechanism. From the above results and discussions, a plausible mechanism for the visible-light photocatalytic H_2 generation has been proposed and illustrated in Figure S6. The organic linker 2-amino terephthalic acid can behave as a visible-light harvester. During the visible-light irradiation, an electron excitation has occurred from the HOMO to the LUMO of the organic linker. Subsequently, the photoexcited electron transferred to the titanium−oxo cluster of MOF by the ligand to cluster charge transfer process (LCCT).[63,64] Furthermore, as demonstrated previously, the photogenerated electrons are rapidly moved to rGO through $\pi-\pi$ interactions, and the photoluminescence and time-resolved studies support this electron transport process. The electron transfer via rGO subsequently involved in the reduction of H^+ ions into H_2 and the photogenerated holes oxidizes the TEOA and produces $TEOA^+$ ions. The importance and existence of the $\pi-\pi$ interaction was clearly verified previously by various studies.

CONCLUSIONS

A simple wet impregnation method was adapted to develop a noncovalently attached NH_2-MIL-125(Ti)/rGO MOF-based photocatalyst. The incorporation of NH_2-MIL-125(Ti) MOF with rGO induced the strong $\pi-\pi$ interaction, and the role of the $\pi-\pi$ interaction in the charge transfer process was evaluated toward the photocatalytic H_2 production activity. Noncovalently attached NH_2-MIL-125(Ti)/rGO MOFs showed that enhanced photocatalytic H_2 production activity through $\pi-\pi$ interaction facilitated the photogenerated electron−hole pair separation. Moreover, the $\pi-\pi$ interaction mediated photocatalytic activity was proved and verified by the screening of the $\pi-\pi$ interaction using PPy. Apart from the superior photocatalytic activity of this material, we believe that the $\pi-\pi$ interaction chemistry mediated charge transport between MOF and graphene could provide a new insight into material design for solar energy conversion.

ASSOCIATED CONTENT

Supporting Information

The Supporting Information is available free of charge on the ACS Publications website at DOI: 10.1021/acsaem.7b00245.

Experimental procedures, including synthesis of NH_2-MIL-125(Ti)/rGO MOF, polypyrrole/rGO, and polypyrrole/rGO-NH_2-MIL-125(Ti) MOF; characterization data, including XRD, GC graphs for H_2 production, UV−vis DRS, Tauc plot, and SEM-EDX; PL and time-resolved studies; mechanism for H_2 production; and tables, including data for BET surface area, lifetime decay, rate constant, and H_2 production comparison (PDF)

AUTHOR INFORMATION

Corresponding Authors

*E-mail: eb.raman@ncl.res.in.

*E-mail: neppolian.b@res.srmuniv.ac.in.

ORCID

Wonyong Choi: 0000-0003-1801-9386

Ekambaram Balaraman: 0000-0001-9248-2809

Notes

The authors declare no competing financial interest.

ACKNOWLEDGMENTS

This work was financially supported by the Science and Engineering Research Board-Department of Science and Technology (SERB-DST) (File EMR/2014/000645) and the Ministry of New and Renewable Energy (MNRE), (File 103/239/2015-NT), DST-Solar Energy Research Initiative (SERI) (File DST/TMD/SERI/S170 (G)), New Delhi, India.

REFERENCES

(1) Grätzel, M. Photoelectrochemical Cells. *Nature* **2001**, *414*, 338−344.

(2) Tilman, D.; Hill, J.; Lehman, C. Carbon-negative Biofuels from Low-input High-diversity Grassland Biomass. *Science* **2006**, *314*, 1598−1600.

(3) Wang, R.; Wu, L.; Chica, B.; Gu, L.; Xu, G.; Yuan, Y. Ni $(dmgH)_2$ Complex Coupled with Metal-Organic Frameworks MIL-101 (Cr) for Photocatalytic H_2 Evolution Under Visible Light Irradiation. *J. Materiomics* **2017**, *3*, 58−62.

(4) Lin, Y.-C.; Huber, G. W. The Critical Role of Heterogeneous Catalysis in Lignocellulosic Biomass Conversion. *Energy Environ. Sci.* **2009**, *2*, 68−80.

(5) Fateeva, A.; Chater, P. A.; Ireland, C. P.; Tahir, A. A.; Khimyak, Y. Z.; Wiper, P. V.; Darwent, J. R.; Rosseinsky, M. J. A Water-Stable Porphyrin-Based Metal−Organic Framework Active for Visible-Light Photocatalysis. *Angew. Chem.* **2012**, *124*, 7558−7562.

(6) Long, J. R.; Yaghi, O. M. The Pervasive Chemistry of Metal−Organic Frameworks. *Chem. Soc. Rev.* **2009**, *38*, 1213−1214.

(7) Liao, P.-Q.; Zhang, W.-X.; Zhang, J.-P.; Chen, X.-M. Efficient Purification of Ethene by an Ethane-Trapping Metal-Organic Framework. *Nat. Commun.* **2015**, *6*, 8697.

(8) Sun, L.; Campbell, M. G.; Dincă, M. Electrically Conductive Porous Metal−Organic Frameworks. *Angew. Chem., Int. Ed.* **2016**, *55*, 3566−3579.

(9) Liu, X.-L.; Wang, R.; Zhang, M.-Y.; Yuan, Y.-P.; Xue, C. Dye-sensitized MIL-101 Metal Organic Frameworks Loaded with Ni/NiO_x Nanoparticles for Efficient Visible-Light-Driven Hydrogen Generation. *APL Mater.* **2015**, *3*, 104403−7.

(10) Seoane, B.; Coronas, J.; Gascon, I.; Benavides, M. E.; Karvan, O.; Caro, J.; Kapteijn, F.; Gascon, J. Metal−Organic Framework Based Mixed Matrix Membranes: A Solution for Highly Efficient CO_2 Capture? *Chem. Soc. Rev.* **2015**, *44*, 2421−2454.

(11) Wang, S.; Morris, W.; Liu, Y.; McGuirk, C. M.; Zhou, Y.; Hupp, J. T.; Farha, O. K.; Mirkin, C. A. Surface-Specific Functionalization of Nanoscale Metal−Organic Frameworks. *Angew. Chem., Int. Ed.* **2015**, *54*, 14738−14742.

DOI: 10.1021/acsaem.7b00245
ACS Appl. Energy Mater. XXXX, XXX, XXX−XXX

(12) Jin, S.; Son, H.-J.; Farha, O. K.; Wiederrecht, G. P.; Hupp, J. T. Energy Transfer from Quantum Dots to Metal−Organic Frameworks for Enhanced Light Harvesting. *J. Am. Chem. Soc.* **2013**, *135*, 955−958.
(13) Sheberla, D.; Bachman, J. C.; Elias, J. S.; Sun, C.-J.; Shao-Horn, Y.; Dincă, M. Conductive MOF Electrodes for Stable Supercapacitors with High Areal Capacitance. *Nat. Mater.* **2017**, *16*, 220−224.
(14) Yuan, Y.-P.; Yin, L.-S.; Cao, S.-W.; Xu, G.-S.; Li, C.-H.; Xue, C. Improving Photocatalytic Hydrogen Production of Metal−Organic Framework UiO-66 Octahedrons by Dye-sensitization. *Appl. Catal., B* **2015**, *168*, 572−576.
(15) Nasalevich, M. A.; Goesten, M. G.; Savenije, T. J.; Kapteijn, F.; Gascon, J. Enhancing Optical Absorption of Metal−Organic Frameworks for Improved Visible Light Photocatalysis. *Chem. Commun.* **2013**, *49*, 10575−10577.
(16) Zhou, T.; Du, Y.; Borgna, A.; Hong, J.; Wang, Y.; Han, J.; Zhang, W.; Xu, R. Post-Synthesis Modification of a Metal−Organic Framework to Construct a Bifunctional Photocatalyst for Hydrogen Production. *Energy Environ. Sci.* **2013**, *6*, 3229−3234.
(17) Alvaro, M.; Carbonell, E.; Ferrer, B.; Llabrés i Xamena, F. X.; Garcia, H. Semiconductor Behavior of a Metal-Organic Framework (MOF). *Chem. - Eur. J.* **2007**, *13*, 5106−5112.
(18) Wu, Y.; Luo, H.; Wang, H. Synthesis of Iron (III)-based Metal−Organic Framework/Graphene Oxide Composites with Increased Photocatalytic Performance for Dye Degradation. *RSC Adv.* **2014**, *4*, 40435−40438.
(19) Wu, Y.; Luo, H.; Zhang, L. Pd Nanoparticles Supported on MIL-101/reduced Graphene Oxide Photocatalyst: An Efficient and Recyclable Photocatalyst for Triphenylmethane Dye Degradation. *Environ. Sci. Pollut. Res.* **2015**, *22*, 17238−17243.
(20) Xu, J.; He, S.; Zhang, H.; Huang, J.; Lin, H.; Wang, X.; Long, J. Layered Metal−Organic Framework/Graphene Nanoarchitectures for Organic Photosynthesis Under Visible Light. *J. Mater. Chem. A* **2015**, *3*, 24261−24271.
(21) Ahmed, I.; Jhung, S. H. Composites of Metal−Organic Frameworks: Preparation and Application in Adsorption. *Mater. Today* **2014**, *17*, 136−146.
(22) Liu, X.-W.; Sun, T.-J.; Hu, J.-L.; Wang, S.-D. Composites of Metal−Organic Frameworks and Carbon-based Materials: Preparations, Functionalities and Applications. *J. Mater. Chem. A* **2016**, *4*, 3584−3616.
(23) Wang, P.; Tang, Y.; Dong, Z.; Chen, Z.; Lim, T.-T. Ag−AgBr/TiO_2/rGO Nanocomposite for Visible-light Photocatalytic Degradation of Penicillin G. *J. Mater. Chem. A* **2013**, *1*, 4718−4727.
(24) Vinoth, R.; Karthik, P.; Muthamizhchelvan, C.; Neppolian, B.; Ashokkumar, M. Carrier Separation and Charge Transport Characteristics of Reduced Graphene Oxide Supported Visible-Light Active Photocatalysts. *Phys. Chem. Chem. Phys.* **2016**, *18*, 5179−5191.
(25) Horiuchi, Y.; Toyao, T.; Saito, M.; Mochizuki, K.; Iwata, M.; Higashimura, H.; Anpo, M.; Matsuoka, M. Visible-Light-Promoted Photocatalytic Hydrogen Production by using an Amino-functionalized Ti (IV) Metal−Organic Framework. *J. Phys. Chem. C* **2012**, *116*, 20848−20853.
(26) Sun, D.; Liu, W.; Fu, Y.; Fang, Z.; Sun, F.; Fu, X.; Zhang, Y.; Li, Z. Noble Metals Can Have Different Effects on Photocatalysis Over Metal−Organic Frameworks (MOFs): A Case Study on M/NH_2-MIL-125 (Ti)(M= Pt and Au). *Chem. - Eur. J.* **2014**, *20*, 4780−4788.
(27) Toyao, T.; Saito, M.; Horiuchi, Y.; Mochizuki, K.; Iwata, M.; Higashimura, H.; Matsuoka, M. Efficient Hydrogen Production and Photocatalytic Reduction of Nitrobenzene Over a Visible-Light-responsive Metal−Organic Framework Photocatalyst. *Catal. Sci. Technol.* **2013**, *3*, 2092−2097.
(28) Wang, Q. H.; Hersam, M. C. Room-temperature Molecular-resolution Characterization of Self-Assembled Organic Monolayers on Epitaxial Graphene. *Nat. Chem.* **2009**, *1*, 206−211.
(29) Ohta, T.; Bostwick, A.; Seyller, T.; Horn, K.; Rotenberg, E. Controlling the Electronic Structure of Bilayer Graphene. *Science* **2006**, *313*, 951−954.
(30) Niyogi, S.; Bekyarova, E.; Itkis, M. E.; Zhang, H.; Shepperd, K.; Hicks, J.; Sprinkle, M.; Berger, C.; Lau, C. N.; Deheer, W. A.; et al. Spectroscopy of Covalently Functionalized Graphene. *Nano Lett.* **2010**, *10*, 4061−4066.
(31) Georgakilas, V.; Otyepka, M.; Bourlinos, A. B.; Chandra, V.; Kim, N.; Kemp, K. C.; Hobza, P.; Zboril, R.; Kim, K. S. Functionalization of Graphene: Covalent and Non-Covalent Approaches, Derivatives and Applications. *Chem. Rev.* **2012**, *112*, 6156−6214.
(32) Karousis, N.; Tagmatarchis, N.; Tasis, D. Current Progress on the Chemical Modification of Carbon Nanotubes. *Chem. Rev.* **2010**, *110*, 5366−5397.
(33) Tasis, D.; Tagmatarchis, N.; Bianco, A.; Prato, M. Chemistry of Carbon Nanotubes. *Chem. Rev.* **2006**, *106*, 1105−1136.
(34) Dan-Hardi, M.; Serre, C.; Frot, T.; Rozes, L.; Maurin, G.; Sanchez, C.; Férey, G. A New Photoactive Crystalline Highly Porous Titanium (IV) Dicarboxylate. *J. Am. Chem. Soc.* **2009**, *131*, 10857−10859.
(35) Wang, H.; Yuan, X.; Wu, Y.; Zeng, G.; Chen, X.; Leng, L.; Wu, Z.; Jiang, L.; Li, H. Facile Synthesis of Amino-functionalized Titanium Metal-Organic Frameworks and their Superior Visible-light Photocatalytic Activity for Cr(VI) Reduction. *J. Hazard. Mater.* **2015**, *286*, 187−194.
(36) Huang, Q.; Tian, S.; Zeng, D.; Wang, X.; Song, W.; Li, Y.; Xiao, W.; Xie, C. Enhanced Photocatalytic Activity of Chemically Bonded TiO_2/Graphene Composites based on the Effective Interfacial Charge Transfer Through the C−Ti Bond. *ACS Catal.* **2013**, *3*, 1477−1485.
(37) Zhang, H.; Lv, X.; Li, Y.; Wang, Y.; Li, J. P25-Graphene Composite as a High Performance Photocatalyst. *ACS Nano* **2010**, *4*, 380−386.
(38) Naumenko, D.; Snitka, V.; Snopok, B.; Arpiainen, S.; Lipsanen, H. Graphene-enhanced Raman Imaging of TiO_2 Nanoparticles. *Nanotechnology* **2012**, *23*, 465703−7.
(39) xxHow, G. T. S.; Pandikumar, A.; Ming, H. N.; Ngee, L. H. Highly Exposed {001} Facets of Titanium Dioxide Modified with Reduced Graphene Oxide for Dopamine Sensing. *Sci. Rep.* **2015**, *4*, 5044.
(40) Otal, E.; Kim, M.; Calvo, M.; Karvonen, L.; Fabregas, I. O.; Sierra, C.; Hinestroza, J. A Panchromatic Modification of the Light Absorption Spectra of Metal−Organic Frameworks. *Chem. Commun.* **2016**, *52*, 6665−6668.
(41) Hu, S.; Liu, M.; Li, K.; Zuo, Y.; Zhang, A.; Song, C.; Zhang, G.; Guo, X. Solvothermal Synthesis of NH_2-MIL-125 (Ti) from Circular Plate to Octahedron. *CrystEngComm* **2014**, *16*, 9645−9650.
(42) Leofanti, G.; Padovan, M.; Tozzola, G.; Venturelli, B. Surface Area and Pore Texture of Catalysts. *Catal. Today* **1998**, *41*, 207−219.
(43) Karthik, P.; Pandikumar, A.; Preeyanghaa, M.; Kowsalya, M.; Neppolian, B. Amino-functionalized MIL-101 (Fe) Metal-Organic Framework as a Viable Fluorescent Probe for Nitroaromatic Compounds. *Microchim. Acta* **2017**, *184*, 2265−2273.
(44) Fu, Y.; Sun, D.; Chen, Y.; Huang, R.; Ding, Z.; Fu, X.; Li, Z. An Amine-Functionalized Titanium Metal−Organic Framework Photocatalyst with Visible-Light-Induced Activity for CO_2 Reduction. *Angew. Chem.* **2012**, *124*, 3420−3423.
(45) Deka, M. J.; Chowdhury, D. Tuning Electrical Properties of Graphene with Different π-stacking Organic Molecules. *J. Phys. Chem. C* **2016**, *120*, 4121−4129.
(46) Sim, L. C.; Leong, K. H.; Ibrahim, S.; Saravanan, P. Graphene Oxide and Ag Engulfed TiO_2Nanotube Arrays for Enhanced Electron Mobility and Visible-Light-Driven Photocatalytic Performance. *J. Mater. Chem. A* **2014**, *2*, 5315−5322.
(47) Xu, Y.; Bai, H.; Lu, G.; Li, C.; Shi, G. Flexible Graphene Films via the Filtration of Water-Soluble Noncovalent Functionalized Graphene Sheets. *J. Am. Chem. Soc.* **2008**, *130*, 5856−5857.
(48) Villar-Rodil, S.; Paredes, J. I.; Martínez-Alonso, A.; Tascón, J. M. Preparation of Graphene Dispersions and Graphene-Polymer Composites in Organic Media. *J. Mater. Chem.* **2009**, *19*, 3591−3593.
(49) Wang, S.; Dong, Y.; He, C.; Gao, Y.; Jia, N.; Chen, Z.; Song, W. The Role of sp^2/sp^3 Hybrid Carbon Regulation in the Nonlinear Optical Properties of Graphene Oxide Materials. *RSC Adv.* **2017**, *7*, 53643−53652.

DOI: 10.1021/acsaem.7b00245
ACS Appl. Energy Mater. XXXX, XXX, XXX−XXX

(50) Wang, A.; Yu, W.; Huang, Z.; Zhou, F.; Song, J.; Song, Y.; Long, L.; Cifuentes, M. P.; Humphrey, M. G.; Zhang, L.; et al. Covalent Functionalization of Reduced Graphene Oxide with Porphyrin by Means of Diazonium Chemistry for Nonlinear Optical Performance. *Sci. Rep.* **2016**, *6*, 23325−12.
(51) Liu, Z.; Liu, J.; Wang, T.; Li, Q.; Francis, P. S.; Barrow, C. J.; Duan, W.; Yang, W. Switching Off the Interactions Between Graphene Oxide and Doxorubicin using Vitamin C: Combining Simplicity and Efficiency in Drug Delivery. *J. Mater. Chem. B* **2018**, *6*, 1251−1259.
(52) Li, Y.; Chen, H.; Voo, L. Y.; Ji, J.; Zhang, G.; Zhang, G.; Zhang, F.; Fan, X. Synthesis of Partially Hydrogenated Graphene and Brominated Graphene. *J. Mater. Chem.* **2012**, *22*, 15021−15024.
(53) Smalley, A. P.; Reid, D. G.; Tan, J. C.; Lloyd, G. O. Alternative Synthetic Methodology for Amide Formation in the Post-Synthetic Modification of Ti-MIL125-NH_2. *CrystEngComm* **2013**, *15*, 9368−9371.
(54) Han, J.-M.; Wu, N.; Wang, B.; Wang, C.; Xu, M.; Yang, X.; Yang, H.; Zang, L. γ Radiation Induced Self-Assembly of Fluorescent Molecules into Nanofibers: AStimuli-Responsive Sensing. *J. Mater. Chem. C* **2015**, *3*, 4345−4351.
(55) Xue, K.; Zhou, S.; Shi, H.; Feng, X.; Xin, H.; Song, W. A Novel Amperometric Glucose Biosensor Based on Ternary Gold Nanoparticles/Polypyrrole/reduced Graphene Oxide Nanocomposite. *Sens. Actuators, B* **2014**, *203*, 412−416.
(56) Enoki, T.; Takai, K. The Edge State of Nanographene and the Magnetism of the Edge-State Spins. *Solid State Commun.* **2009**, *149*, 1144−1150.
(57) Joly, V. J.; Takahara, K.; Takai, K.; Sugihara, K.; Enoki, T.; Koshino, M.; Tanaka, H. Effect of Electron Localization on the Edge-State Spins in a Disordered Network of Nanographene Sheets. *Phys. Rev. B: Condens. Matter Mater. Phys.* **2010**, *81*, 115408−6.
(58) Su, C.; Acik, M.; Takai, K.; Lu, J.; Hao, S.-j.; Zheng, Y.; Wu, P.; Bao, Q.; Enoki, T.; Chabal, Y. J.; Ping Loh, K. Probing the Catalytic Activity of Porous Graphene Oxide and the Origin of this Behaviour. *Nat. Commun.* **2012**, *3*, 1298−9.
(59) Rao, S.; Stesmans, A.; Noyen, J.; Jacobs, P.; Sels, B. ESR Evidence for Disordered Magnetic Phase from Ultra-Small Carbon Nanotubes Embedded in Zeolite Nanochannels. *EPL (Europhysics Letters)* **2010**, *90*, 57003−5.
(60) Joly, V. J.; Kiguchi, M.; Hao, S.-J.; Takai, K.; Enoki, T.; Sumii, R.; Amemiya, K.; Muramatsu, H.; Hayashi, T.; Kim, Y. A.; et al. Observation of Magnetic Edge State in Graphene Nanoribbons. *Phys. Rev. B: Condens. Matter Mater. Phys.* **2010**, *81*, 245428−6.
(61) Wang, J.; Wang, H.; Wang, Y.; Li, J.; Su, Z.; Wei, G. Alternate Layer-by-Layer Assembly of Graphene Oxide Nanosheets and Fibrinogen Nanofibers on a Silicon Substrate for a Biomimetic Three-Dimensional Hydroxyapatite Scaffold. *J. Mater. Chem. B* **2014**, *2*, 7360−7368.
(62) Fan, W.; Lai, Q.; Zhang, Q.; Wang, Y. Nanocomposites of TiO_2 and reduced Graphene Oxide as Efficient Photocatalysts for Hydrogen Evolution. *J. Phys. Chem. C* **2011**, *115*, 10694−10701.
(63) Han, Y.; Han, L.; Zhang, L.; Dong, S. Ultrasonic Synthesis of Highly Dispersed Au Nanoparticles Supported on Ti-based Metal−Organic Frameworks for Electrocatalytic Oxidation of Hydrazine. *J. Mater. Chem. A* **2015**, *3*, 14669−14674.
(64) Zhang, G.; Kim, G.; Choi, W. Visible Light Driven Photocatalysis Mediated via Ligand-to-Metal Charge Transfer (LMCT): An Alternative Approach to Solar Activation of Titania. *Energy Environ. Sci.* **2014**, *7*, 954−966.

DOI: 10.1021/acsaem.7b00245
ACS Appl. Energy Mater. XXXX, XXX, XXX−XXX

π-π Interaction Between Metal-Organic Framework and Reduced Graphene Oxide for Visible Light Photocatalytic H_2 Production

Peramaiah Karthik,[a] Ramalingam Vinoth,[a] Peng Zhang,[c] Wonyong Choi,[c] Ekambaram Balaraman,[b]* and Bernaurdshaw Neppolian[a]*

[a] SRM Research Institute, SRM University, Kattankulathur, Chennai-603203, Tamil Nadu, India.

[b]Catalysis Division, CSIR-National Chemical Laboratory (CSIR-NCL), Dr. Homi Bhabha Road, Pune-411008, India.

[c]Division of Environmental Science and Engineering, Pohang University of Science and Technology (POSTECH), Pohang, 37673, Korea.

*Corresponding Authors: eb.raman@ncl.res.in; neppolian.b@res.srmuniv.ac.in

Contents List

Section S1: General Information

Chemicals and Reagents

Graphite flakes (particle size +100 mesh (Z75% min)) were purchased from Sigma Aldrich. Analytical grade titanium tetraisopropoxide and 2-Amino terephthalic acid were purchased from SRL, chemicals, India and Alfa aesar. All other reagents and solvents were of analytical grade and were used as received without any further purification.

Section S2: Preparation of Graphene oxide (GO)

Graphene oxide (GO) was prepared from graphite powder by modified hummers method.[S1] typically, 2 g graphite powder and 1 g of $NaNO_3$ were mixed with 46 mL of conc. H_2SO_4. Then the mixture was stirred for 30 min in ice bath. While stirring, 2 g of $KMnO_4$ was added to the suspension and the temperature was maintained around 20°C. Subsequently, 92 mL of deionized water added to the reaction mixture and stirred for 30 min at 98°C. After that, an appropriate amount of H_2O_2 (3%) was added to the reaction mixture until the appearance of effervescence stopped. The solid product was washed with deionized water for several times to remove the impurities. Finally, the obtained GO was freeze-dried under vacuum.

Section S3: Synthesis of NH_2-MIL-125(Ti)/rGO by hydrothermal method

The NH_2-MIL-125(Ti) MOF was synthesized by hydrothermal method. In brief, 2.4 mL of titanium tetra isopropoxide (TTIP), 2.2 g of 2-aminoterephthalic acid and calculated amount of GO were added into DMF – methanol mixture (36 and 4mL). The resulting solution was

transferred into 100 mL Teflon-lined stainless-steel autoclave and heated at 150 °C for 48 h. After that the resultant precipitate was collected by centrifugation and repeatedly washed with methanol to remove the un-reacted DMF. Finally, the obtained powder was dried at 180°C for 12 h to remove the residual 2-aminoterephthalic acid.

Section S4: Photoelectrochemical measurements:

The samples casted glassy carbon (GC) electrodes were prepared by following procedures: 0.2 mL ethanol dispersion with samples (~3 mg) mixed with 0.01 mL of Nafion (Sigma-Aldrich) under ultrasonic process (10 min) to form a homogenous suspension. 0.01 mL above suspension was added onto the surface of GC electron and dry in ambient condition. The electrochemical measurements were carried out in beaker by using an electrochemical workstation (IVIUM technologies) in a three-electrode system devised of a modified GC, a Ag/AgCl electrode, and a Pt wire as working, counter and reference electrodes, respectively. All of the measurements were carried out in 0.2 M Na_2SO_4 at room temperature.

Section S5: Apparent Quantum Yield (AQY)

The AQY of photocatalytic H_2 production activity was calculated by using 420 nm band pass filter. The irradiation area was calculated as 0.00144 m^2

AQY Calculation details

The energy of one photon (E_{photon}) with wavelength of λ_{inc} (nm) was calculated using the literature method.[S3]

Section S6: Synthesis of polypyrrole/rGO

The polypyrrole/rGO composite was synthesized by following reported method with slight modification. 50 mg of rGO was depressed in water and HCl mixture (18 mL H_2O +1.74 mL HCl). After sonication of 1h, 1.3 mL of pyrrole monomer was added above solution. Subsequently, 2.28 g of ammonium persulfate (APS) solution (dissolved in 10 mL of water) was also added and the resultant mixture was stirred for 24 h at 100 ºC. Finally, the suspension was separated, washed with DI water and dried at 80 °C for 12 h

Section S7: Synthesis of polypyrrole/rGO-NH_2-MIL-125(Ti) MOF

Polypyrrole/rGO-NH_2-MIL-125(Ti) MOF was also synthesized by similar wet impregnation method using polypyrrole/rGO instead of rGO. In brief, 300 mg of NH_2-MIL-125(Ti) MOF was dispersed in water by using ultrasonicator. To this, 18 mg of polypyrrole/rGO was added. Afterward, the resultant suspension was sonicated for 30 min (20 kHz, low frequency ultrasonicator, continuous mode, amplitude 30%). Finally, the mixture was pre-dried in a hot plate and impregnated powder was dried in an oven at 180°C for 24 h.

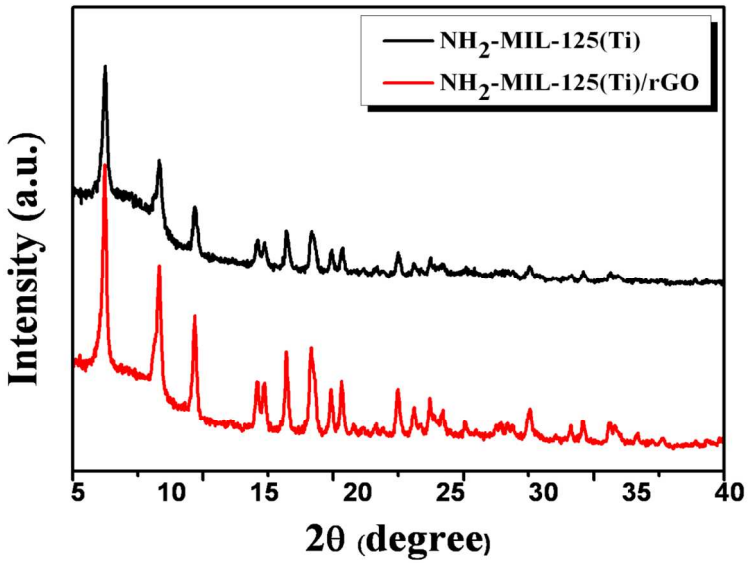

Figure S1. XRD patterns of NH_2-MIL-125(Ti) and NH_2-MIL-125(Ti)/rGO MOF.

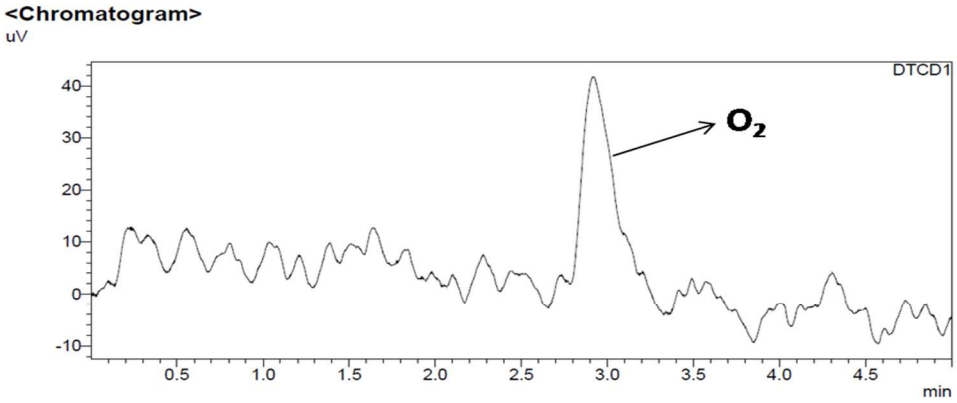

Figure S2. GC graph of photocatalytic H_2 production using PPy/rGO-NH_2-MIL-125(Ti) MOF.

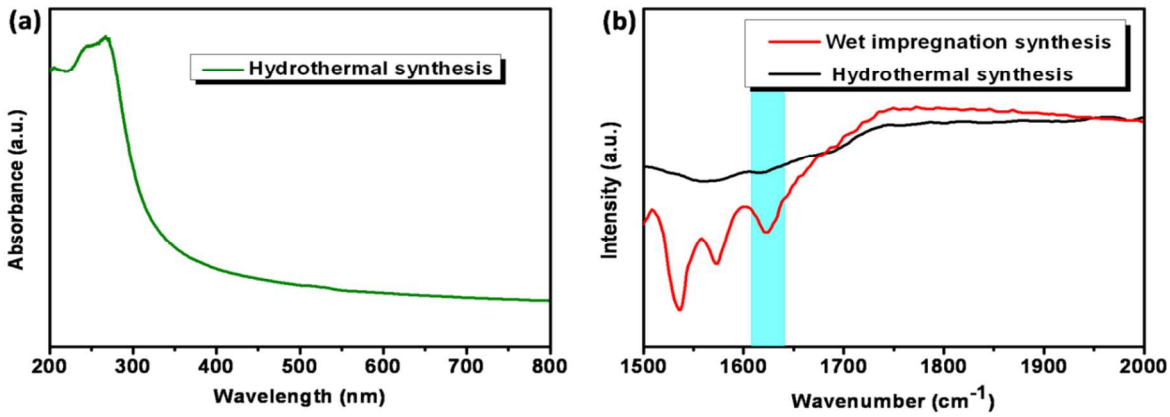

Figure S3. (a)UV-Vis absorbance spectra of hydrothermally synthesized rGO supported NH_2-MIL-125(Ti) MOF. (b) FTIR spectra of NH_2-MIL-125(Ti)/rGO synthesized by hydrothermal and wet impregnation.

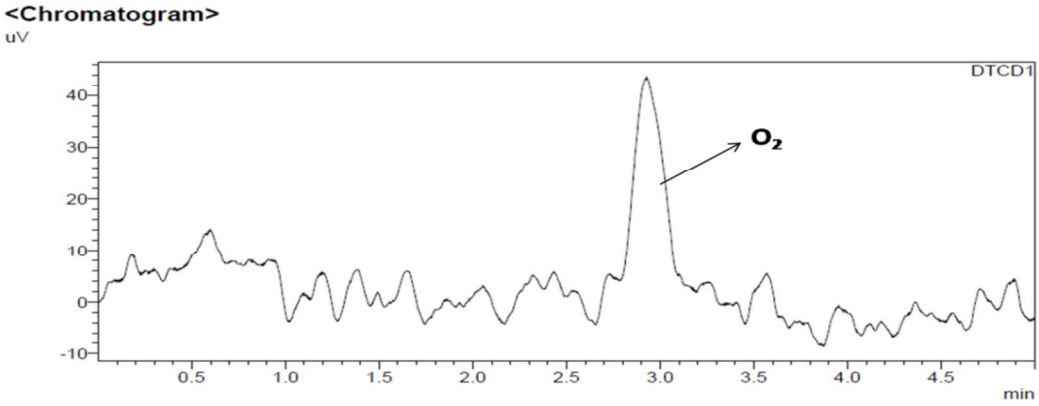

Figure S4. GC graph of photocatalytic H_2 production using hydrothermally synthesized NH_2-MIL-125(Ti)/rGO.

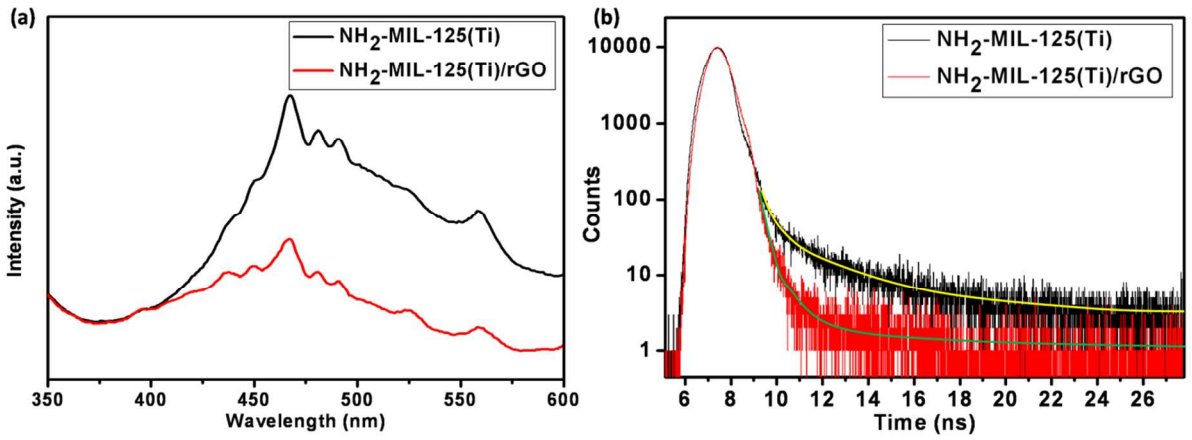

Figure S5. (a) PL spectra of NH_2-MIL-125(Ti) and NH_2-MIL-125(Ti)/rGO MOFs excited at 380 nm. (b) Time-resolved PL decay profiles for NH_2-MIL-125(Ti) and NH_2-MIL-125(Ti)/rGO.

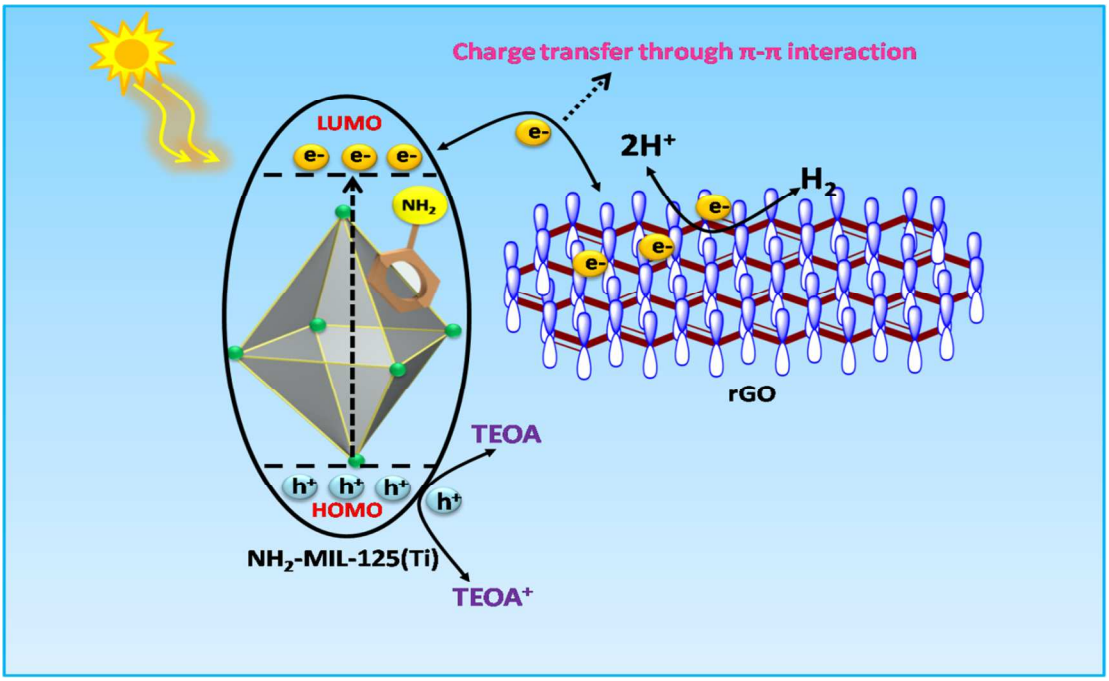

Figure S6. Possible mechanism for photocatalytic H_2 production under visible-light irradiation.

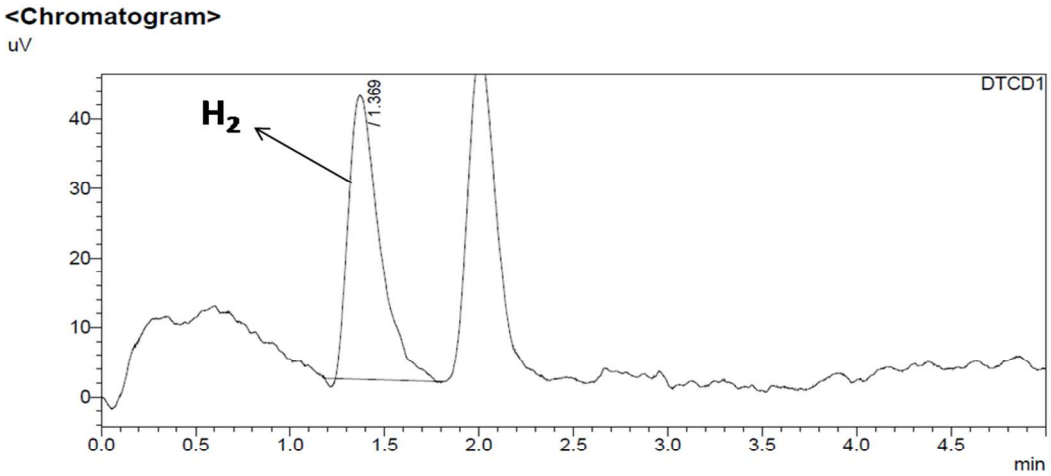

<Peak Table>

DTCD1

Peak#	Ret. Time	Area	Area%	Height	Height%	Name
1	1.369	469	100.000	41	100.000	
Total		469	100.000	41	100.000	

Figure S7. GC graph of photocatalytic H_2 production using synthesized NH_2-MIL-125(Ti)/ rGO.

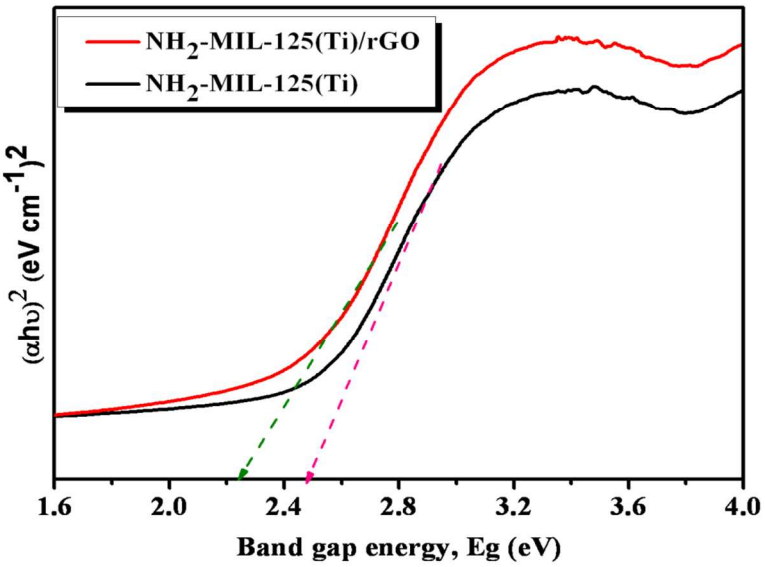

Figure S8. Tauc plot of NH_2-MIL-125(Ti) and NH_2-MIL-125(Ti)/rGO.

The band-gap energy values of photocatalyst were calculated using Tauc's plot method (Figure S8) using the energy dependent correlation of hv = $(hv-Eg)^{1/2}$, where and Eg are the absorption coefficient and the energy gap value of a semiconducting materials.[S4-S5] As can be seen from Figure S8, the calculated band gap value of NH_2-MIL-125(Ti) and NH_2-MIL-125(Ti)/rGO MOFs are 2.6 and 2.2 eV, respectively. The decrease in the band-gap of NH_2-MIL-125(Ti)/rGO MOF is due to the formation of bonds through free π-electrons of rGO and the empty orbitals of Ti-oxo-cluster and the similar observation was also observed elsewhere.[S6-S7]

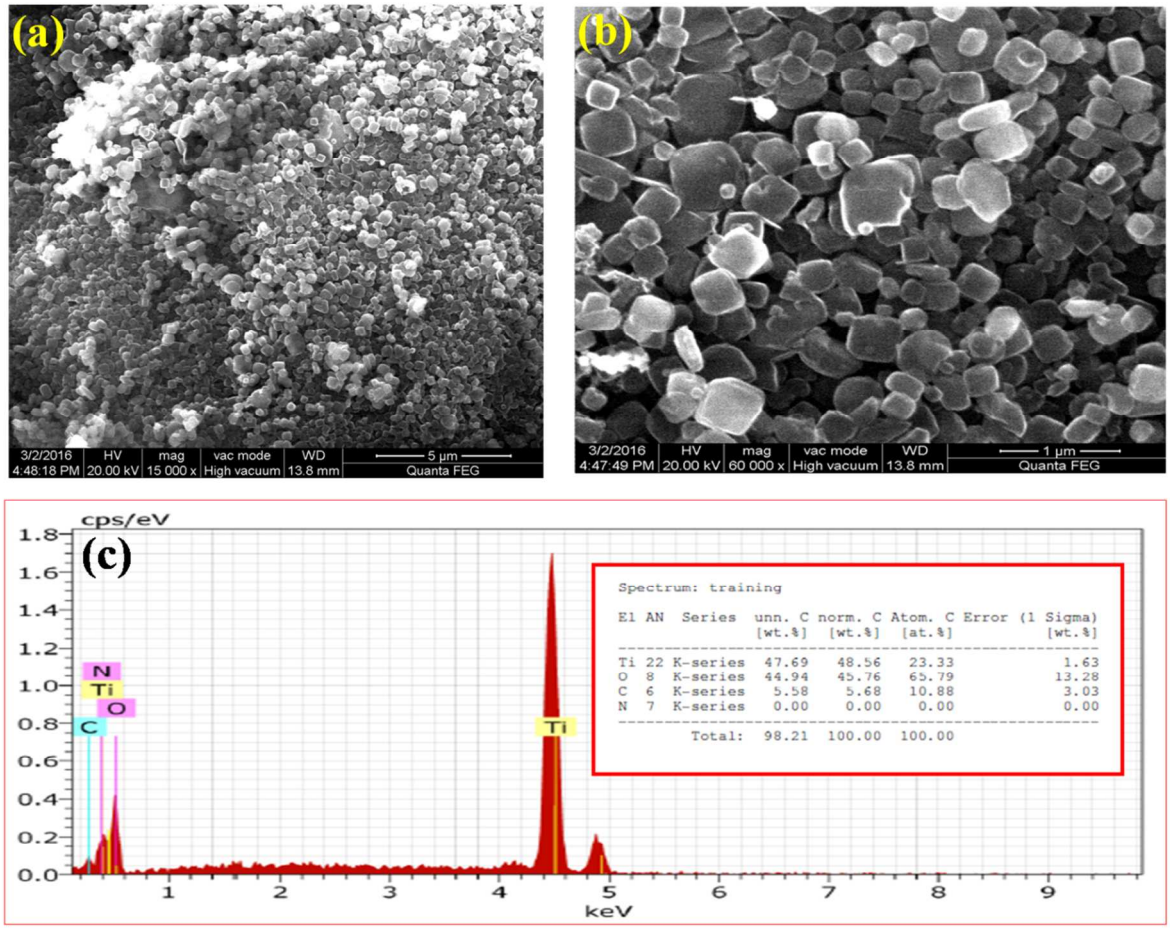

Figure S9. (a) and (b) SEM images and (c) SEM-EDX analysis of NH_2-MIL-125(Ti)/rGO.

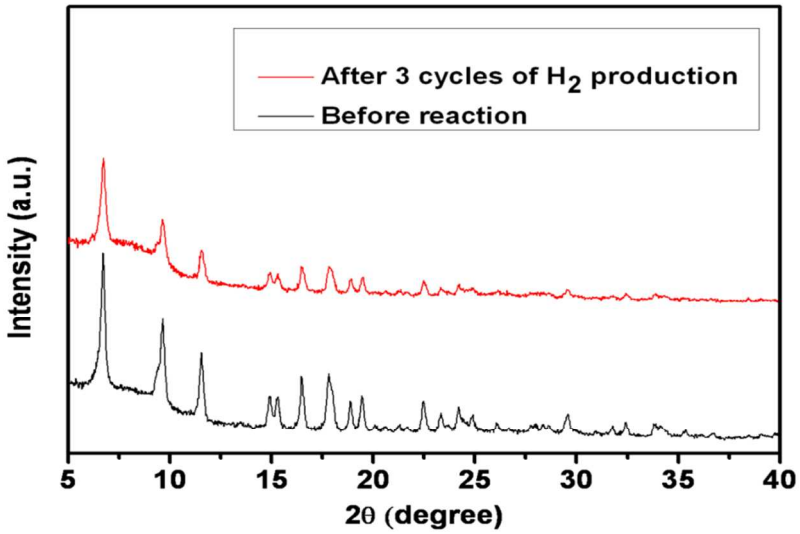

Figure S10. XRD pattern of NH_2-MIL-125(Ti)/rGO MOF after photocatalytic H_2 production reaction.

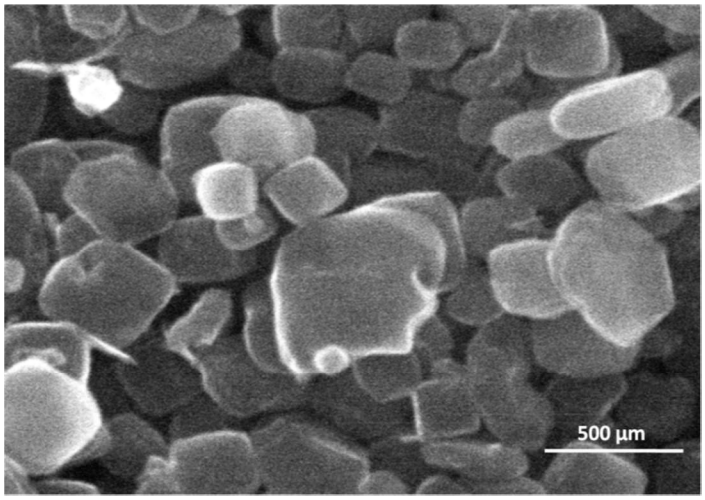

Figure S11. SEM image ofNH_2-MIL-125(Ti)/rGO MOF after photocatalytic H_2 production reaction.

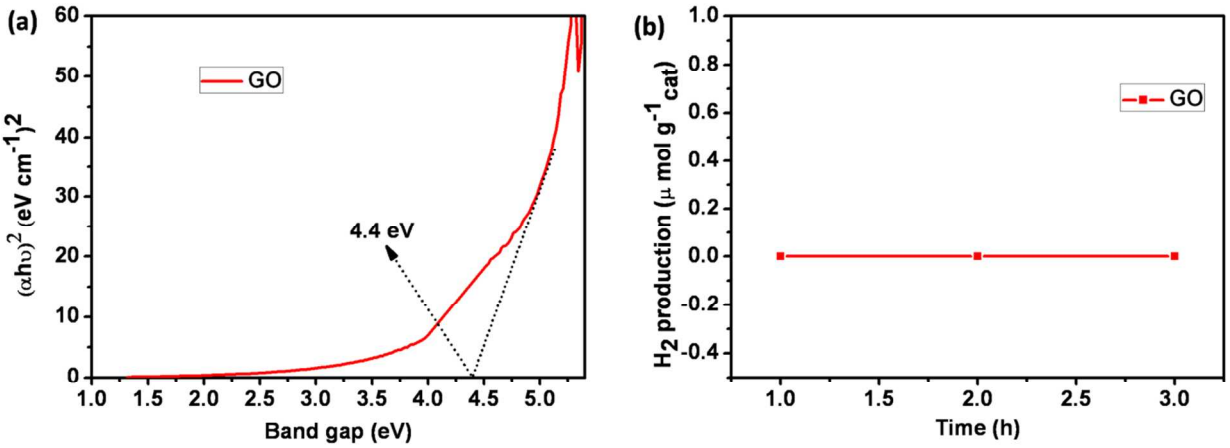

Figure S12. (a) Tau plot for graphene oxide, (b) photocatalytic H_2 production reaction using GO as photocatalysts (No H_2 evaluation was observed with GO under visible light illumination due to its wide band gap energy (4.2 eV)).

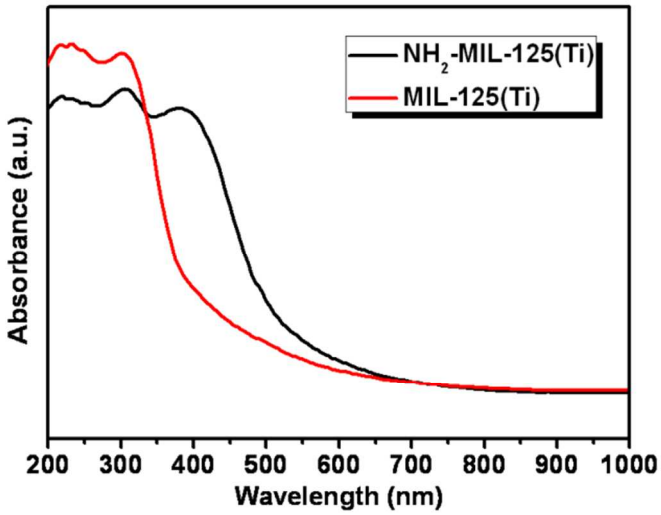

Figure S13. UV-Vis DRS spectra of MIL-125(Ti) MOF

Table S1. BET surface area analysis of MOFs

Name of samples	S_{BET} (m^2 g^{-1})	Pore volume (cc/g)
NH_2-MIL-125(Ti)	710	0.649
NH_2-MIL-125(Ti)/6wt%rGO	962	0.266

Table S2. % of C=C calculated from C1S spectra

MOFs	Peak type	FWHM	% of C=C
NH_2-MIL-125(Ti)	Gaussian	1.4	30.66
NH_2-MIL-125(Ti)/rGO	Gaussian	1.1	40.78 %

Table S3. Kinetic rate constant for production of H_2 using various NH_2-MIL-125(Ti)/GO photocatalysts.

Name of samples	Rate constant (k)/min
NH_2-MIL-125(Ti)	0.052
NH_2-MIL-125(Ti)/2wt%rGO	0.285
NH_2-MIL-125(Ti)/4wt%rGO	0.399
NH_2-MIL-125(Ti)/6wt%rGO	**0.748**
NH_2-MIL-125(Ti)/8wt%rGO	0.550
NH_2-MIL-125(Ti)/10wt%rGO	0.538

Table S4. Comparison on the photocatalytic performance of different MOFs based photocatalysts for photocatalytic H_2 production.

Sl. No	Photocatalyst	Co-Catalysts	Light source	Reaction solution	H_2 production	AQE	Ref
1	Pt-Ti-NH_2 MOF	Pt	300 W Xe lamp	Water + TEOA	33 µ mol	---	*S8*
2	Pt/NH_2-Uio-66(Zr/Ti)	Pt	300 W Xe lamp	Water + TEOA	3.5µmol$h^{-1}$$gcat^{-1}$	---	S9
3	Ti-MOF-Ru(tpy)	Ru	300 W Xe lamp	Water + TEOA	10.9 µmol$h^{-1}$$gcat^{-1}$	0.2 % at 500 nm	S10
4	RhB/Pt@UiO-66(Zr)-100	Pt	300 W Xe lamp	Water + TEOA	116.1µmol $h^{-1}$$gcat^{-1}$	---	S11
5	Ag(1.5)/Gd-MOF	---	300 W Xe lamp	Water + TEOA	10.6 µmol$h^{-1}$$gcat^{-1}$	---	S12
6	MOF-253-Pt	Pt	300W Xe lamp	TEOA	100-200	1.63 % at 440 nm	S13
7	Al/Zn-PMOF	Pt	300 W Xe lamp	EDTA solution	200 µmol$h^{-1}$$gcat^{-1}$	0.1 %	S14

8	Co@NH_2-MIL-125(Ti)	Co	500W Xe/Hg lamp	TEOA	37 µ mol	0.5 %	S15
9	[CoII(TPA)Cl][Cl]-MIL-125-NH_2	Co	200 W Xelamp	CH3CN and TEOA	553 µmol $g^{-1}h^{-1}$	---	S16
10	Pt@CdS/MIL-101(Cr)	Pt	300W Xe lamp	lactic acid	150 µmol $g^{-1}h^{-1}$	---	S17
11	**NH_2-MIL-125(Ti)/rGO (6 wt % rGO)**	**---**	**300 W Xe lamp**	**Water +TEOA**	**91**	**0.66 % at 420 nm**	**This work**

Table S5. Life time decay data.

Sample	A1	η_1 (ns)	A2	η_2 (ns)
NH_2-MIL-125(Ti)	13.8%	0.96	51.2 %	3.5
NH_2-MIL-125(Ti)/rGO	12.9%	0.88	14.7%	1.07

References

1. Hummers Jr, W. S.; Offeman, R. E. Preparation of Graphitic Oxide. *J. Am. Chem. Soc.* **1958,** *80*, 1339-1339.

2. Sun, W.; Wang, L.; Wu, T.; Wang, M.; Yang, Z.; Pan, Y.; Liu, G. Inhibiting the Corrosion-Promotion Activity of Graphene. *Chem. Mater.* **2015,** *27,* 2367-2373.

3. Yu, Y.-G.; Chen, G.; Hao, L.-X.; Zhou, Y.-S.; Wang, Y.; Pei, J.; Sun, J.-X.; Han, Z.-H. Doping La into the Depletion Layer of The $Cd_{0.6}Zn_{0.4}S$ Photocatalyst for Efficient H_2 Evolution. *Chem. Commun* .**2013,** *49*, 10142-10144.

4. Meng, Z.-D.; Zhu, L.; Ghosh, T.; Park, C.-Y.; Ullah, K.; Nikam, V.; Oh, W.-C. Ag_2Se-Graphene/TiO_2 Nanocomposites, Sonochemical Synthesis and Enhanced Photocatalytic Properties Under Visible Light. *Bull. Korean Chem. Soc* .**2012,** *33*, 3761-3766.

5. Hendon, C. H.; Tiana, D.; Fontecave, M.; Sanchez, C. m.; D'arras, L.; Sassoye, C.; Rozes, L.; Mellot-Draznieks, C.; Walsh, A., Engineering the Optical Response of the Titanium-MIL-125 Metal–Organic Framework Through Ligand Functionalization. *J. Am. Chem. Soc.* **2013,** *135*, 10942-10945.

6. Wang, P.; Wang, J.; Wang, X.; Yu, H.; Yu, J.; Lei, M.; Wang, Y. One-step Synthesis of Easy-Recycling TiO_2-rGO Nanocomposite Photocatalysts with Enhanced Photocatalytic Activity. *Appl. Catal. B: Environ.* **2013,** *132*, 452-459.

7. Liu, H.; Lv, T.; Wu, X.; Zhu, C.; Zhu, Z. Preparation and Enhanced Photocatalytic Activity of CdS@ rGO Core–Shell Structural Microspheres. *Appl. Surf. Sci.* **2014,** *305*, 242-246.

8. Horiuchi, Y.; Toyao, T.; Saito, M.; Mochizuki, K.; Iwata, M.; Higashimura, H.; Anpo, M.; Matsuoka, M. Visible-Light-Promoted Photocatalytic Hydrogen Production by using an Amino-functionalized Ti(IV) Metal–Organic Framework. *J. Phys. Chem. C* **2012,** *116*, 20848-20853.

9. Sun, D.; Liu, W.; Qiu, M.; Zhang, Y.; Li, Z. Introduction of a Mediator for Enhancing Photocatalytic Performance via Post-Synthetic Metal Exchange in Metal–Organic Frameworks(MOFs). *Chem. Commun.* **2015,** *51*, 2056-2059.

10. Toyao, T.; Saito, M.; Dohshi, S.; Mochizuki, K.; Iwata, M.; Higashimura, H.; Horiuchi, Y.; Matsuoka, M. Development of a Ru Complex-Incorporated MOF Photocatalyst for Hydrogen Production Under Visible-Light Irradiation. *Chem. Commun.* **2014,** *50*, 6779-6781.

11. He, J.; Wang, J.; Chen, Y.; Zhang, J.; Duan, D.; Wang, Y.; Yan, Z. A Dye-Sensitized Pt@ UiO-66(Zr) Metal–Organic Framework for Visible-Light Photocatalytic Hydrogen Production. *Chem. Commun.* **2014,** *50*, 7063-7066.

12. Sun, X.; Yu, Q.; Zhang, F.; Wei, J.; Yang, P. A Dye-Like Ligand-Based Metal–Organic Framework for Efficient Photocatalytic Hydrogen Production from Aqueous Solution. *Catal. Sci. Tech.* **2016,** *6*, 3840-3844.

13. Zhou, T.; Du, Y.; Borgna, A.; Hong, J.; Wang, Y.; Han, J.; Zhang, W.; Xu, R. Post-Synthesis Modification of a Metal–Organic Framework to Construct a Bifunctional Photocatalyst for Hydrogen Production. *Energy Environ. Sci.* **2013,** *6*, 3229-3234.

14. Fateeva, A.; Chater, P. A.; Ireland, C. P.; Tahir, A. A.; Khimyak, Y. Z.; Wiper, P. V.; Darwent, J. R.; Rosseinsky, M. J. A Water-Stable Porphyrin-Based Metal–Organic Framework Active for Visible-Light Photocatalysis. *Angew. Chem.* **2012,** *124*, 7558-7562.

15. Nasalevich, M. A.; Becker, R.; Ramos-Fernandez, E. V.; Castellanos, S.; Veber, S. L.; Fedin, M. V.; Kapteijn, F.; Reek, J. N.; Van Der Vlugt, J.; Gascon, J. Co@ NH_2-MIL-125(Ti): Cobaloxime-Derived Metal–Organic Framework-Based Composite for Light-Driven H_2Production. *Energy Environ. Sci.* **2015,** *8*, 364-375.

16. Li, Z.; Xiao, J.-D.; Jiang, H.-L. Encapsulating a Co(II) Molecular Photocatalyst in Metal–Organic Framework for Visible-Light-Driven H_2 Production: Boosting Catalytic Efficiency via Spatial Charge Separation. *ACS Catal.* **2016,** *6*, 5359-5365.

17. He, J.; Yan, Z.; Wang, J.; Xie, J.; Jiang, L.; Shi, Y.; Yuan, F.; Yu, F.; Sun, Y. Significantly Enhanced Photocatalytic Hydrogen Evolution Under Visible Light Over CdS Embedded on Metal–Organic Frameworks. *Chem. Commun.* **2013,** *49*, 6761-6763.